

This additional Electronic Supplementary Information file published on 24 Jun 2021 is an updated version of the article originally published on 23 Jan 2020 (available at <https://doi.org/10.1039/C9CP06284J>) that incorporates the changes detailed in the corresponding correction article (DOI: 10.1039/D1CP90126E).

## ARTICLE

# The corrosion inhibition of stainless steel by ferrocene-polyoxometalate hybrid molecular materials – experimental and first principles studies

Received 20th November 2019,  
Accepted 10th January 2020

DOI: 10.1039/c9cp06284j

Corrected manuscript

G. Sruthi<sup>a</sup>, K. Shakeela<sup>b</sup>, R. Shanmugam<sup>a</sup> and G. Ranga Rao<sup>a\*</sup>

The hybrid molecular materials  $[\text{Fe}(\text{C}_5\text{H}_5)_2]_3[\text{PW}_{12}\text{O}_{40}] \cdot (\text{H}_2\text{O})_4$  and  $[\text{Fe}(\text{C}_5\text{H}_5)_2]_3[\text{PMo}_{12}\text{O}_{40}] \cdot (\text{H}_2\text{O})_6$ , denoted respectively as FcPW and FcPMo, are synthesized *via* a co-precipitation method under acidic conditions (pH: ~2-3). The molecular properties of these compounds are investigated *via* various analytical methods. UV-vis diffuse reflectance and photoluminescence studies confirm that these compounds are charge transfer salts. Stainless steel plates (SS, 316 grade) coated with these hybrid compounds and dipped in 0.5 M  $\text{H}_2\text{SO}_4$  and Ringer's solutions show significantly inhibited corrosion. The corrosion inhibition property of these materials is studied *via* weight loss, electrochemical impedance spectroscopy and potentiodynamic polarization studies. The reproducibility of the corrosion inhibition results is ensured *via* repeated measurements, and error values are reported. The surfaces of the corroded steel plates are examined *via* scanning electron and atomic force microscopy techniques. It is found that the corrosion is of uniform type. The Tafel extrapolation method shows that the inhibition efficiency is 74% for SS@FcPMo and 65% for SS@FcPW. The corrosion inhibition mechanism is explained based on the redox nature of the hybrid materials. The experimental results are corroborated by computational studies carried out using first principles with optimized geometries and frontier molecular orbitals of the hybrid molecular materials.

**Keywords:** Ferrocenium, Keggin, Corrosion inhibition, Stainless Steel, First principles

## Introduction

Corrosion is a global problem for any metallic structure and material, and it has become one of the most prevailing issues that need to be addressed in the present times. During the course of corrosion, there is considerable deterioration of materials used in

equipment, and the costs incurred in replacing the corroded parts have escalated over the years. It is imperative, therefore, to produce novel and more corrosion-resistant coatings that are cheaper, more effective and easier to use. Corrosion can be of several types, namely, uniform, crevice, pitting, stress, etc.<sup>1</sup> Among these, stainless steel is more prone to crevice, uniform and pitting corrosion. Crevice corrosion occurs through a differential  $\text{O}_2$  cell, whereas uniform and pitting corrosion take place by the breakdown of oxide films. Stainless steel differs from mild steel in terms of the chromium content. The chromium present in the steel allows passivation by forming an inert chromium oxide layer.<sup>2,3</sup> Different grades of stainless steel have different compositions; of these, grades 316 and 317 are resistant to attack by low concentrations of sulphuric acid, whereas grade 304 is not resistant to sulphuric acid.<sup>3,4</sup> It is well known that grade 316 stainless steel provides excellent resistance to most of the chemical and non-chemical environments. However, it still does not offer effective resistance especially in the food industry toward low pH products. Hence, there is always demand to develop

<sup>a</sup>Department of Chemistry and DST-IITM Solar Energy Harnessing Centre (DSEHC) Indian Institute of Technology Madras, Chennai 600036, India

<sup>b</sup>Department of Chemistry, B.S. Abdur Rahman Crescent Institute of Science and Technology, Vandalur, Chennai 600048, India

\*Corresponding author; Tel.: +91 44 2257 4226; Fax: +91 44 2257 4202; E-mail address: [grrao@iitm.ac.in](mailto:grrao@iitm.ac.in) (G. Ranga Rao).

Electronic Supplementary Information (ESI) available: [It contains eclipsed and staggered conformations of ferrocene in Fig. S1. Steady state open circuit potential vs. time for 6 min after stabilization for bare SS, SS@FcPW and SS@FcPMo is shown in Fig. S2. <sup>31</sup>P MAS spectra of FcPW and FcPMo hybrid materials is given in Fig. S3. Nyquist and Tafel plots of SS, SS@FcPW, SS@FcPMo with Ringer's solution as electrolyte are provided in Fig. S5, with parameters for calculating corrosion rate and inhibition efficiency in Tables S3 and S4. Nyquist, Tafel plots and calculations based on triplicate experiments of corrosion studies in 0.5 M  $\text{H}_2\text{SO}_4$  and Ringer's solution are provided in Figs. S4, S6 and Table S2, S5. Textural parameters of FcPW and FcPMo are given in Table S1. Structural parameters (bond lengths, bond angles and torsional angles between atoms) of optimized structures in FcPW and FcPMo hybrid materials are provided in Tables S6-S11.]. See DOI: 10.1039/c9cp06284j

better and more effective corrosion-resistant materials for certain specific processing operations in the food industry.<sup>5,6</sup> For this purpose, several hybrid materials containing inorganic and/or organic moieties have been developed and tested for corrosion inhibition over the years.<sup>7-9</sup>

Inorganic-organic hybrid materials containing ferrocene and/or polyoxometalates have been explored for several decades, but the development of novel hybrid materials continues to engage scientists to explore their emerging properties and useful applications. Ferrocene  $[\text{Fe}(\text{C}_5\text{H}_5)_2]$  is an iron containing metallocene existing in both eclipsed ( $D_{5h}$ ) and staggered ( $D_{5d}$ ) conformations, but present predominantly in staggered form (Fig. S1 of ESI). The eclipsed conformation of ferrocene has five planes of symmetry perpendicular to the cyclopentadienyl rings ( $5\sigma_v$ ), with additional plane of symmetry sandwiched between the two rings and passing through Fe atom ( $\sigma_h$ ). Since only null vector  $\vec{0}$  is transformed onto itself by all these planes of symmetry, the eclipsed conformation of ferrocene has a dipole moment of zero. In the case of staggered conformation, apart from the five planes of symmetry perpendicular to the ring planes ( $5\sigma_v$ ), there is also a centre of symmetry in the Fe atom ( $i$ ) as well as improper rotation ( $S_{10}$ ). The inversion centre alone determines that the null vector  $\vec{0}$  transforms upon itself. Therefore, the staggered form of ferrocene also has no dipole moment.<sup>10</sup> Ferrocene has an electron donor-acceptor conjugated structure and is an efficient redox couple of  $\text{Fe}^{2+}/\text{Fe}^{3+}$ . Further, it is non-toxic, lipophilic and insoluble in water. In the presence of an oxidizing agent, such as  $\text{H}_2\text{SO}_4$ , oxidation of  $[\text{Fe}(\text{C}_5\text{H}_5)_2]$  to  $[\text{Fe}(\text{C}_5\text{H}_5)_2]^+$  (ferrocenium cation) occurs, which is characterized by deep red coloration.<sup>11,12</sup> The well-known applications of ferrocene include sensing,<sup>13</sup> corrosion,<sup>7,14</sup> catalysis,<sup>15</sup> and energy conversion.<sup>16,17</sup>

Polyoxometalates (POMs) are polyatomic compounds in which transition metal (like Mo, W) containing anions are linked together in a 3D framework through shared and terminal oxygen atoms. Although it is known that metal oxides and polyoxoion salts are water-insoluble, the polyoxometalates comprising early transition elements are readily soluble in water. There are two types of polyoxometalates – isopolyanions having general formula  $[\text{M}_m\text{O}_y]^{p-}$ , and heteropolyanions having formula  $[\text{X}_x\text{M}_m\text{O}_y]^{q-}$  (for  $x \leq m$ ), where X is heteroatom or oxyanion (P, Si,

etc.) and M is the metal ion. M is referred to as an addenda atom, having favorable ionic radius and charge, with the ability to form  $d\pi - p\pi$  M–O bonds. It is usually molybdenum, tungsten, or in few cases, vanadium, niobium or tantalum in their highest oxidation states.<sup>18,19</sup> Heteropolyacids, containing transition metal-oxygen anions, have been well studied for several decades in catalysis,<sup>20-22</sup> corrosion,<sup>8</sup> sensing,<sup>23</sup> energy conversion,<sup>24</sup> energy storage,<sup>25,26</sup> cytotoxicity,<sup>27</sup> and water remediation.<sup>28</sup> They are efficient corrosion inhibitors, with low toxicities compared to the more popular chromates.<sup>29</sup> There have been reports in the literature on the synthesis of various charge transfer salts of polyoxometalates with ferrocene.<sup>30-34</sup> The formation of charge-transfer salt occurs as a result of redox behaviour of both the polyoxometalates and ferrocene. The saturated valence metals in polyoxometalates form intensely blue mixed-valence species called heteropoly blues. These heteropoly blues, in turn, can act as reducing agents and can change back to their polyoxometalate form.<sup>20,35,36</sup> The polyoxometalates in the presence of organic donors undergo self-assembly process form organic-inorganic hybrid materials.<sup>37,38</sup>

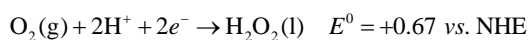
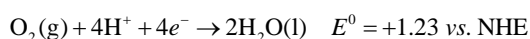
In the present study, we have synthesized hybrid materials, (1) ferrocene salt with phosphomolybdic acid (FcPMo) and (2) ferrocene salt with phosphotungstic acid (FcPW), which show unique redox and catalytic properties. The as-synthesized hybrid molecular materials are essentially charge transfer salts comprising ferrocenium ion and polyoxometalate anion. Ferrocene, which oxidizes to form ferrocenium ion in the presence of  $\text{H}_2\text{SO}_4$ , which acts as an oxidizing agent, interacts with the Keggin moiety of the polyoxometalate to form charge transfer salts. The use of an acidic medium in the synthesis of hybrids is imperative considering the stability of the polyoxometalates, especially of the Keggin type ( $[\text{PW}_{12}\text{O}_{40}]^{3-}$ ,  $[\text{PMo}_{12}\text{O}_{40}]^{3-}$ ) in low pH range of 2 to 3.<sup>20</sup> Other metallocenes such as cobaltocene were not explored as they are less stable in air and the presence of moisture, and they are very reactive at temperatures slightly above the ambient. The ferrocenium ion  $[\text{Fe}(\text{C}_5\text{H}_5)_2]^+$ , generated in  $\text{H}_2\text{SO}_4$ , co-precipitates with phosphotungstic acid (PWA) and phosphomolybdic acid (PMoA) to form FcPW and FcPMo hybrid materials, respectively. The molecular formulae of the resulting hybrid materials are predicted to be  $[\text{Fe}(\text{C}_5\text{H}_5)_2]_3[\text{PW}_{12}\text{O}_{40}] \cdot (\text{H}_2\text{O})_4$  and  $[\text{Fe}(\text{C}_5\text{H}_5)_2]_3[\text{PMo}_{12}\text{O}_{40}] \cdot (\text{H}_2\text{O})_6$  based on spectroscopic studies, which will be discussed later. These hybrid molecular materials are studied for their corrosion resistance properties in

partnership with stainless steel (316 grade; SS316). The types of corrosion which can affect SS316 include uniform corrosion, when  $\text{H}_2\text{SO}_4$  is used as the electrolyte, and pitting corrosion when  $\text{HCl}$  is used the electrolyte. We used 0.5 M  $\text{H}_2\text{SO}_4$  electrolyte for corrosion studies. For uniform corrosion, the reactions involved at the anode and cathode are as follows:

Anodic reaction:  $\text{Fe(s)} \rightarrow \text{Fe}^{2+}(\text{aq}) + 2\text{e}^-$

Cathodic reaction:  $2\text{H}^+(\text{aq}) + 2\text{e}^- \rightarrow \text{H}_2(\text{g})$

A passive film formed on the surface of stainless steel protects it against corrosion, and this is composed of  $\text{Fe}_2\text{O}_3$ ,  $\text{Fe}(\text{OH})_3$  and  $\text{Cr}_2\text{O}_3$ .<sup>14,39,40</sup> There exists, however, a distinct possibility for oxygen reduction reaction (ORR) to interfere with the cathodic reaction involving hydrogen evolution. In acidic medium, ORR proceeds *via* two reaction pathways: (1) 4  $\text{e}^-$  transfer from  $\text{O}_2$  to  $\text{H}_2\text{O}$  or (2) 2  $\text{e}^-$  transfer from  $\text{O}_2$  to  $\text{H}_2\text{O}_2$ .<sup>41-43</sup>



The ORR interference is minimized by purging the electrolyte solution with  $\text{N}_2$  or Ar gas to remove most of the dissolved oxygen.

## Materials and Methods

Ferrocene (Spectrochem India), phosphotungstic acid ( $\text{H}_3\text{PW}_{12}\text{O}_{40} \cdot x\text{H}_2\text{O}$ ) (Sisco Research Laboratories) and phosphomolybdic acid ( $\text{H}_3\text{PMo}_{12}\text{O}_{40} \cdot 24\text{H}_2\text{O}$ ) (Thermo Fisher Scientific) were used for the synthesis of the hybrid materials. For acidic medium,  $\text{H}_2\text{SO}_4$  (Merck India) was used in the synthesis and for corrosion inhibition studies. All the purchased materials were used without further purification unless otherwise stated.

The FTIR spectra were recorded using JASCO FT/IR 4100 spectrometer in the range 400–4000  $\text{cm}^{-1}$ . UV-Visible diffuse reflectance spectra for the solid samples were recorded using JASCO V-660 UV-visible spectrometer. The samples were analyzed *via* powder X-ray diffraction using BRUKER AXS D8 advanced diffractometer at room temperature with Cu  $\text{K}\alpha$  radiation ( $\lambda = 1.54 \text{ \AA}$ ). The  $^{31}\text{P}$  MAS NMR spectra of phosphotungstic acid, phosphomolybdic acid and their hybrid salts with ferrocene were recorded using Bruker Avance 400 spectrometer with resonance frequency 161.97 MHz for  $^{31}\text{P}$  nuclei. The chemical shifts (ppm,  $\delta$ ) are recorded relative to 85 wt%  $\text{H}_3\text{PO}_4$ .<sup>44</sup> The SEM images were taken by depositing finely powdered samples on carbon tape and examining them under FEI Quanta 450 microscope operating at 30 kV in low vacuum. CHN analysis of the samples was done using the 2400 Series II analyser. PL spectra were recorded using Horiba

Jobin Yvon Fluoromax-4 fluorescence spectrophotometer. Negative ion MALDI-TOF-MS(–) was recorded using Bruker Flex series using DHB (2,5-dihydroxybenzoic acid) as matrix. Inductively coupled plasma optical emission spectroscopy (ICP-OES) was recorded using Perkin Elmer Optima 5300 DV. Vibrating sample magnetometer (VSM) of Lakeshore, USA, Model 7407 with maximum magnetic field: 2.5 T and dynamic moment range of  $1 \times 10^{-6} \text{ emu}$  to  $10^3 \text{ emu}$  was used to record the variation of magnetization of material as a function of varying magnetic field at room temperature. Atomic force microscopy (AFM) in non-contact mode using Model XE-100 (Park Systems) was used for analyzing the extent of corrosion in the corroded samples.

To understand the effects of the molecular geometries and frontier molecular orbitals of FcPW and FcPMo materials on the steel corrosion, plane-wave self-consistent field calculations were performed using a generalized gradient approximation (GGA). In the wave function, Perdew–Burke–Ernzerhof (PBE) with ultrasoft pseudopotential (USPP) was used to describe the exchange–correlation energy. The kinetic cut-off energy of 70 Ry with the convergence criteria of  $1 \times 10^{-6} \text{ eV/\AA}$  and a  $2 \times 2 \times 3$  mesh grid  $k$ -points were applied in geometry optimisation. All the calculations were carried out using Quantum ESPRESSO 6.2.<sup>45</sup> The structural parameters of the optimized structures were analysed using Mercury 3.10.1.

## Synthesis of hybrid molecular materials

Charge transfer complexes of ferrocene with heteropolyacids were synthesized using a method reported in literature.<sup>11</sup> Briefly, 0.5 g of ferrocene was dissolved in 10 mL of 98%  $\text{H}_2\text{SO}_4$  to generate ferrocenium ion (with  $\text{Fe}^{\text{III}}$ ) in a red solution with blue fluorescence. This solution was stirred for 1 h; following this, it was diluted with water to 150 mL and 0.043 M PWA or PMoA solution was added. The stirring was continued for 3 h at room temperature, maintaining the pH between 2 and 3. After 3 h, a precipitate of greenish-blue and greyish blue were obtained, respectively, for ferrocene salt with phosphomolybdic acid (FcPMo) and ferrocene salt with phosphotungstic acid (FcPW). This precipitate differs from the heteropoly blue solutions which are formed when polyoxometalates undergo reduction as a result of their oxidizing properties. The precipitates formed are solid-state hybrid molecular materials that are stable in the pH range of the parent POM. The scheme for synthesis is shown in Fig. 1.

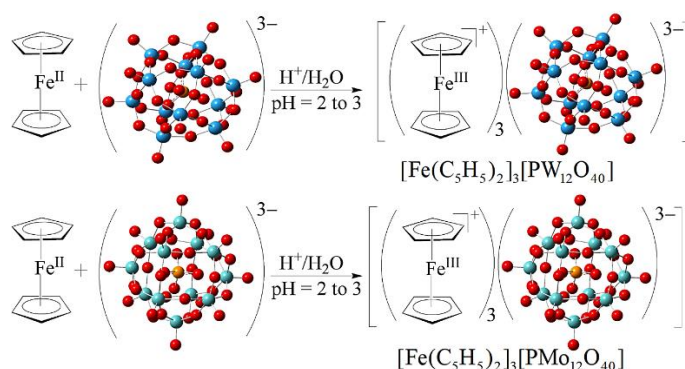


**Figure 1** The synthesis of hybrid molecular materials containing ferrocene and heteropolyacids (PWA and PMoA).

The ferrocenium cation interacts with the anionic cluster of POM by replacing  $H^+$  ions *via* ion exchange to form charge transfer hybrid salt. The Keggin structure self-assembles in acidic aqueous solution to interact with the ferrocenium ion. Self-assembly refers to transition from a disordered state to an ordered state with an overall reduction in entropy.<sup>37,38,46</sup> Thus, the resulting hybrid complexes are formed as a result of charge transfer between the phosphotungstate or phosphomolybdate anion and ferrocene with the molecular formulae  $[Fe(C_5H_5)_2]_3[PW_{12}O_{40}] \cdot xH_2O$  and  $[Fe(C_5H_5)_2]_3[PMo_{12}O_{40}] \cdot yH_2O$ . Due to the self-assembly of POM in acidic solution, there are significant changes in their charge-transfer properties, which are facilitated through anion- $\pi$  interactions between terminal oxygen atoms in the Keggin structure and the cyclopentadienyl ligands.<sup>11</sup>

### Corrosion inhibition studies of the hybrid materials

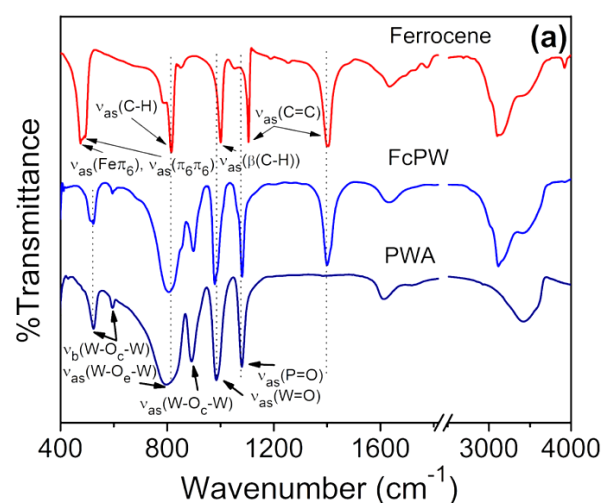
For corrosion inhibition studies, weight loss, cyclic voltammetry (CV), electrochemical impedance spectroscopy (EIS) and Tafel data were recorded with stainless steel (316 grade) plates. Rectangular specimens of 316 grade SS with dimensions 5 cm  $\times$  1 cm and an exposed area 1 cm<sup>2</sup> were mechanically abraded with sandpaper of grit size 3000, and 5/0 grade emery paper. The composition of 316 grade steel is Fe (60–62%), C (<0.08%), Cr (16–18%), Ni (10–14%), Mo (2–3%), Mn (<2%), Si (<1%), P (<0.045%), S (<0.03%); molecular weight = 56.0 g mol<sup>-1</sup>; density = 7.87 g/cm<sup>3</sup> (ASTM F138).<sup>5,47</sup> The area of an electrode immersed in 0.5 M H<sub>2</sub>SO<sub>4</sub> is 1 cm<sup>2</sup>. The weight loss method was used to obtain preliminary results with respect to corrosion inhibition of stainless steel. The weight loss was measured by immersing (a) bare stainless steel plate, (b) a stainless steel plate coated with FcPMo and (c) a

stainless steel plate coated with FcPW in 0.5 M H<sub>2</sub>SO<sub>4</sub> for 24 h. After immersion, the steel samples were taken out, washed with distilled water, dried and weighed again to determine the weight loss. For CV, EIS and Tafel plots, the working electrode used was stainless steel (316 grade) plate coated with FcPMo/FcPW, with a Pt strip counter electrode and Ag/AgCl reference electrode in saturated KCl. These electrodes were used in a 3-electrode cell with electrolyte as 0.5 M H<sub>2</sub>SO<sub>4</sub>. The electrodes were immersed in 0.5 M H<sub>2</sub>SO<sub>4</sub>, and potentiometric measurements were done for 20 min for achieving steady state open circuit potential (OCP); this OCP was checked for next 6 min (Fig. S2, ESI). For the bare steel plate, steel plate coated with the hybrid materials FcPW and FcPMo, EIS were recorded in the frequency range 100 kHz to 0.01 Hz at OCP by setting the AC sine wave amplitude at 5 mV. For the Tafel plots, potentiodynamic polarization curves were obtained in the potential range of –200 to +200 mV with respect to OCP at a scan rate of 2 mV/s. For all electrochemical measurements, the electrolyte was purged with N<sub>2</sub> gas for 30 min to remove the dissolved oxygen, which may affect the cathodic reaction through oxygen reduction reaction (ORR) mechanism. The dissolved oxygen content was measured using Hach Company HQ40D Multipurpose Meter and maintained at a minimum level of 6.5 to 7 ppm.

## 3. Results and Discussion

### Characterization of hybrid materials

The hybrid molecular hybrids are characterized using FTIR, UV-Vis DRS, powder XRD, <sup>31</sup>P MAS spectra, PL spectra, TGA, magnetization, SEM, MALDI-TOF-MS and ICP-OES studies. The FTIR spectra of ferrocene, phosphotungstic acid, phosphomolybdic acid, FcPW and FcPMo are shown in Fig. 2.



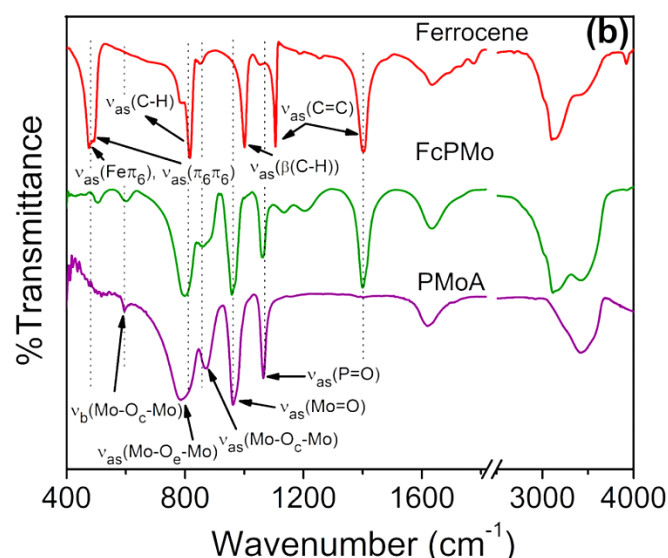


**Figure 2** The FTIR spectra for (a) ferrocene, FcPW and PWA; and (b) ferrocene, FcPMo and PMoA.

The characteristic absorption bands of ferrocene are  $3095\text{ cm}^{-1}$  [ $\nu_{\text{as}}(\text{C-H})$ ];  $1405, 1103\text{ cm}^{-1}$  [ $\nu_{\text{as}}(\text{C}=\text{C})$ ];  $1000\text{ cm}^{-1}$  [ $\nu_{\text{as}}(\beta(\text{C-H}))$ ];  $818\text{ cm}^{-1}$  [ $\nu_{\text{as}}(\text{C-H})$ ] and  $475\text{ cm}^{-1}$  [ $\nu_{\text{as}}(\text{Fe}\pi_6), \nu_{\text{as}}(\pi_6\pi_6)$ ].<sup>11</sup> The band at  $475\text{ cm}^{-1}$  indicates that ferrocene used as precursor and the one in the hybrid are both mixtures of eclipsed ( $D_{5d}$ ) and staggered ( $D_{5h}$ ) forms.<sup>10</sup> The Keggin signature of PWA shows vibrations at  $810\text{ cm}^{-1}$  [ $\nu_{\text{as}}(\text{W-O}_c\text{-W})$ ];  $895\text{ cm}^{-1}$  [ $\nu_{\text{as}}(\text{P=O})$ ] and  $981\text{ cm}^{-1}$  [ $\nu_{\text{as}}(\text{W=O})$ ].<sup>11,19</sup> The absorption bands at  $1078\text{ cm}^{-1}$  and  $1630\text{ cm}^{-1}$  (significantly weakened  $\nu_{\text{as}}(\text{C}=\text{C})$ ) implies the existence of ferrocenium cation in FcPW. The Keggin signature peaks of PMoA are observed at  $790\text{ cm}^{-1}$  [ $\nu_{\text{as}}(\text{Mo-O}_c\text{-Mo})$ ];  $870\text{ cm}^{-1}$  [ $\nu_{\text{as}}(\text{P=O})$ ] and  $961\text{ cm}^{-1}$  [ $\nu_{\text{as}}(\text{Mo=O})$ ].<sup>44</sup> The absorption bands at  $1616$  and  $1063\text{ cm}^{-1}$  (significantly weakened  $\nu_{\text{as}}(\text{C}=\text{C})$ ) imply the existence of ferrocenium cation in FcPMo. Thus, Keggin signature peaks, as well as ferrocene characteristic peaks, can be seen in the hybrids, indicating that the cationic and anionic moieties are intact.

The UV-vis DRS of ferrocene, phosphotungstic acid, phosphomolybdic acid, FcPW and FcPMo are shown in Fig. 3.

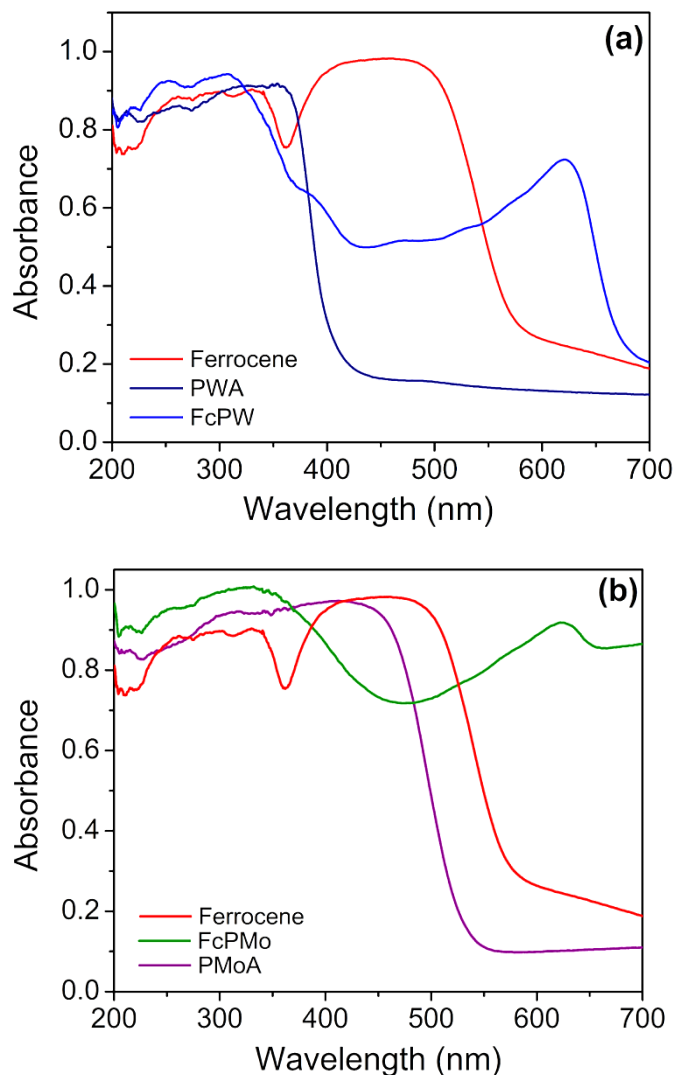


**Figure 3** The UV-vis spectra for (a) ferrocene, FcPW and PWA; and (b) ferrocene, FcPMo and PMoA.

Ferrocene has absorption bands around 330 and 470 nm due to ligand field bands arising from splitting of the  $d$  levels of  $\text{Fe}^{2+}$ .<sup>11</sup> The hybrid materials FcPW and FcPMo each display an absorption band at *ca.* 220–450 nm due to charge transfer from  $\text{O}^{2-}$  to  $\text{W}^{6+}/\text{Mo}^{6+}$  at  $\text{W}=\text{O}$  (or  $\text{Mo}=\text{O}$ ) and  $\text{W-O-W}$  (or  $\text{Mo-O-Mo}$ ) bonds.<sup>11</sup> Further, there is a characteristic broad absorption band at *ca.* 620 nm, which is due to charge transfer from ferrocene to polyoxometalate ion. Also, this peak is closer to the  $\lambda_{\text{max}}$  of  $[\text{Fe}(\text{C}_5\text{H}_5)_2]^+$ .<sup>11,31,33</sup> This charge transfer is further confirmed from PL spectra for ferrocene, phosphotungstic acid, phosphomolybdic acid, and the hybrid materials FcPMo and FcPW as shown in Fig. 4.

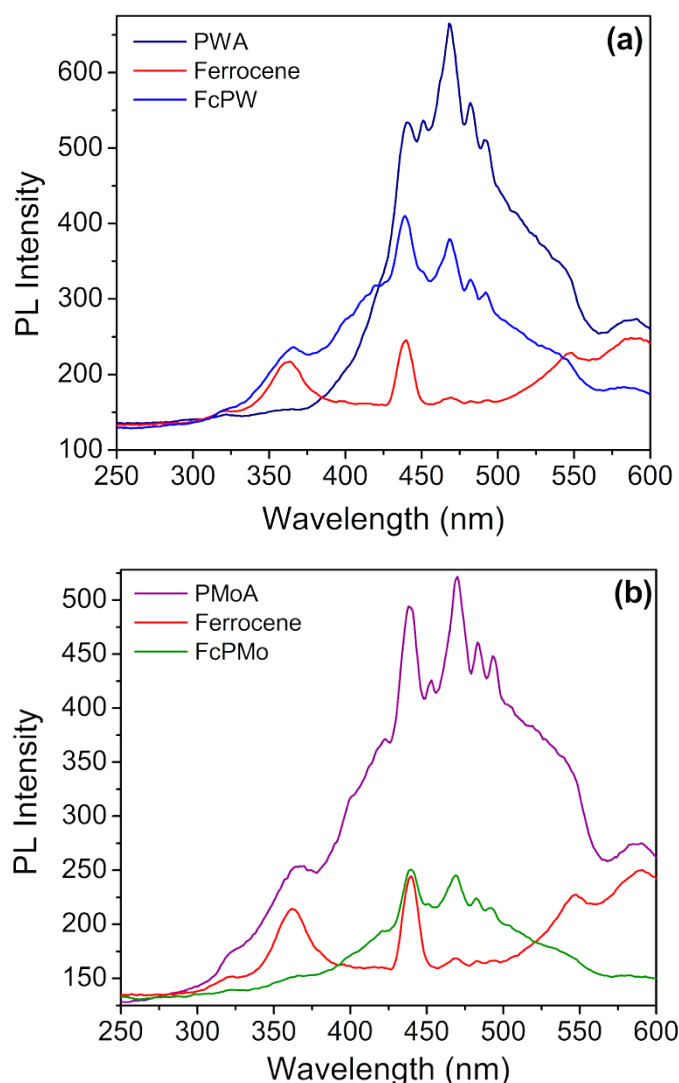


**Figure 4** The photoluminescence spectra for (a) ferrocene, FcPW and PWA; and (b) ferrocene, FcPMo and PMoA.

On exciting light of wavelength 230 nm, and the emission spectra from 230 to 600 nm were recorded. There is a weak emission band corresponding to  $\pi \rightarrow \pi^*$  transition for  $[\text{Fe}(\text{C}_5\text{H}_5)_2]$  in the hybrids FcPMo and FcPW. Also, there are broad emission bands around 395 nm due to O2p to W5d charge transfer. The emission band around 440 nm of FcPW exhibited strong fluorescence signal, while that of FcPMo was found to be quenched. This could be attributed to strong interaction between ferrocene and POM species due to their close proximity. Hence, we say that the binding of  $[\text{Fe}(\text{C}_5\text{H}_5)_2]$  with anionic polyoxometalate is held due to Columbic forces. The fluorescence signals in these charge-transfer salts are distinct, that is, they are either strengthened, weakened, or quenched.<sup>30</sup>

The Tauc plots shown in Fig. 5 are obtained using the equation:  $(\alpha h\nu)^{1/n} = K(h\nu - E)$  where  $K$  is the constant relative to material,  $n$  is 1/2 for direct band gap, and 2 for indirect band gap.<sup>48</sup> Direct band gaps for ferrocene, FcPW and FcPMo were found to be 2.07, 2.98, 1.86 eV, respectively. This indicates that the FcPW hybrid material is active in UV region, while FcPMo is active in the visible light region. Using this information, these hybrid materials can be explored for photocatalytic applications.<sup>11</sup>

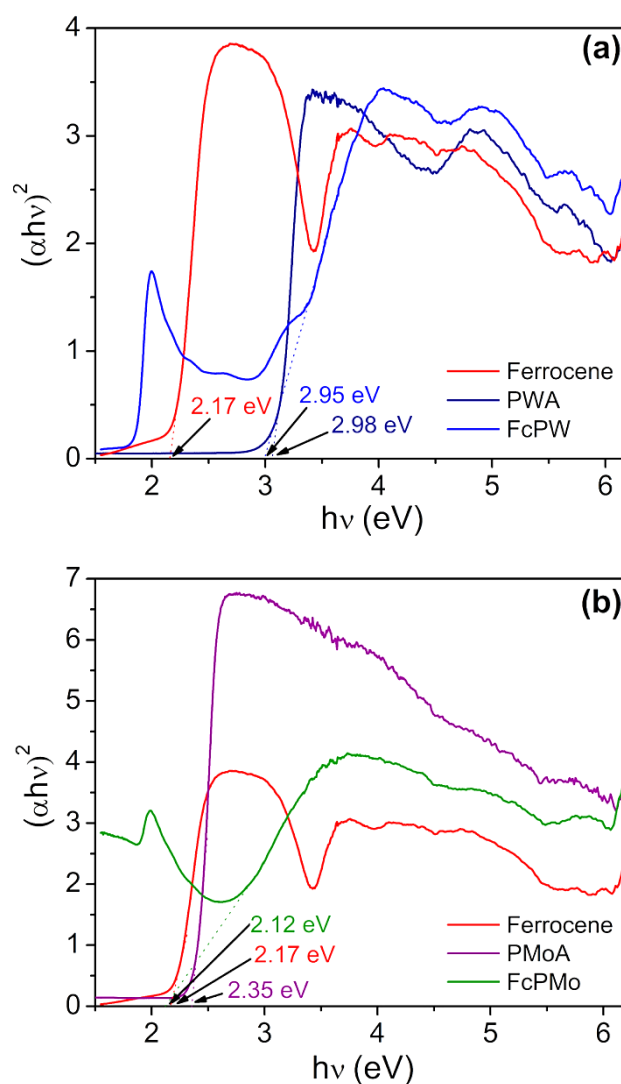


**Figure 5** The Tauc plots for (a) ferrocene, FcPW and PWA; and (b) ferrocene, FcPMo and PMoA.

Powder XRD spectra are recorded and are shown in Fig. 6. The peaks obtained in the hybrid for low angle measurements indicate layered structure. For FcPW, the  $2\theta$  values obtained are  $7.8^\circ$ ,  $8.7^\circ$  and  $9.3^\circ$ , corresponding to (110), (011) and ( $\bar{1}01$ ) of  $[\text{H}_3\text{PW}_{12}\text{O}_{40}]$  (JCPDS 50-0656) peaks at lower angle



measurements, and  $2\theta$  values at  $17.6^\circ$  and  $18.9^\circ$  correspond to (001) and  $(\bar{1}11)$  of ferrocene (JCPDS 29-1711), respectively. Hence, the phosphotungstate anions in the precursor  $[\text{H}_3\text{PW}_{12}\text{O}_{40}]$  (JCPDS 75-2125) have a different crystal structure to those found in the hybrid. This could be attributed to interaction between ferrocene and POM anions resulting in poorly crystalline hybrid FcPW. For FcPMo, the  $2\theta$  values obtained are  $8.5^\circ$ ,  $8.9^\circ$  and  $9.7^\circ$  correspond to  $(\bar{1}\bar{1}1)$ ,  $(0\bar{1}1)$  and  $(\bar{1}01)$  of  $[\text{H}_3\text{PMo}_{12}\text{O}_{40}]$  (JCPDS 75-1588), and  $2\theta$  values at  $15.3^\circ$  and  $17.6^\circ$  correspond to  $(\bar{1}10)$  and (001) of ferrocene (JCPDS 29-1711).

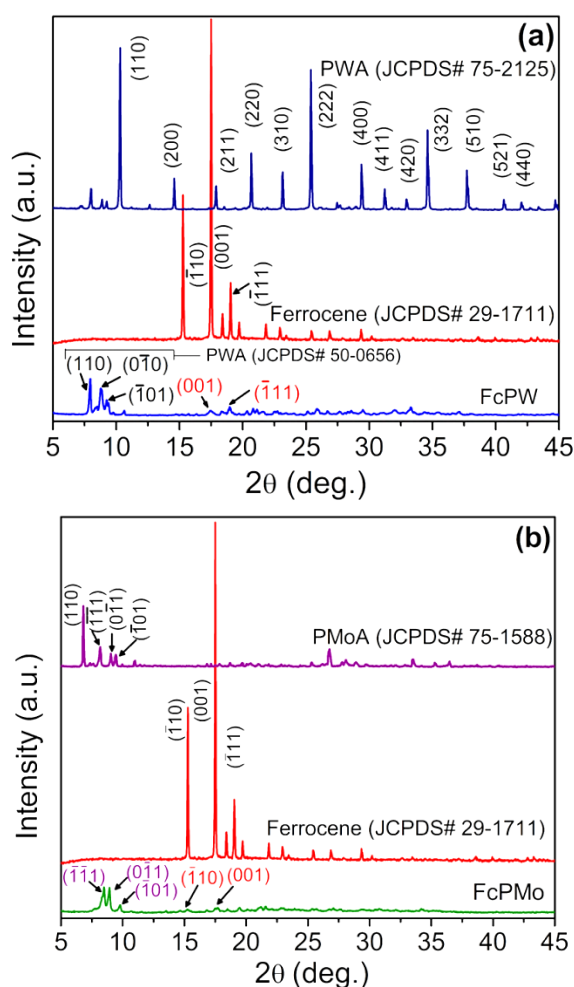


**Figure 6** PXRD plots for (a) ferrocene, FcPW and PWA; and (b) ferrocene, FcPMo and PMoA.

SEM analyses at show uniform surface morphologies with small aggregates clustered together for both the hybrid salts, FcPW and FcPMo (Fig. 7).

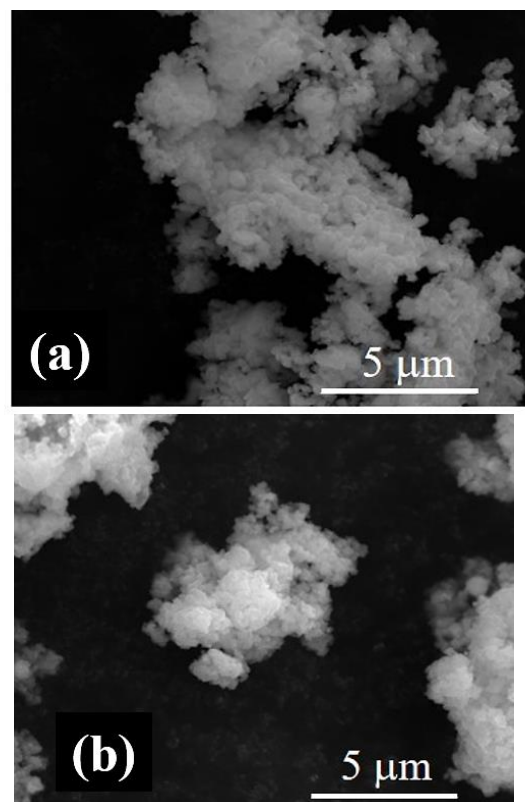


**Figure 7** SEM images of hybrid salt of (a) ferrocene and phosphotungstic acid; and (b) ferrocene and phosphomolybdic acid.

The  $^{31}\text{P}$  MAS NMR spectra in Fig. S3 (ESI) show that phosphotungstic acid has  $^{31}\text{P}$  peak at  $-14.6$  ppm and phosphomolybdic acid has  $^{31}\text{P}$  peak at  $-4.3$  ppm. These values concur with those reported in the literature.<sup>28,44</sup> There are slight shifts in the peaks to  $-14.9$  ppm  $-4.8$  ppm in FcPW and FcPMo, respectively, caused due to interaction of ferrocenium ion with  $\text{PW}_{12}$  and  $\text{PMo}_{12}$  units. Apart from these peaks, additional peaks at  $20.7$  ppm in FcPW and  $-29.9$  ppm in FcPMo are observed. These are due to attributed to interaction between  $[\text{Fe}(\text{C}_5\text{H}_5)_2]^+$  and  $[\text{PMo}_{12}\text{O}_{40}]^{3-}$  ionic species in addition to water loss, resulting in new P-O-P linkages.<sup>49</sup> The positive shift in FcPW could be attributed to phosphorous oxide resulting from decomposition of phosphotungstic acid.<sup>49</sup> MALDI-TOF-MS(−) shows peaks at  $m/z$  values for  $[\text{PW}_{12}\text{O}_{40}]^{3-}$  (obs. 956.5, calc. 955.6) and  $[\text{PMo}_{12}\text{O}_{40}]^{3-}$  (obs. 606.7, calc. 607.5). CHN analysis of the hybrid FcPMo shows obs. (wt.%): C (15.15%), H (0.76%), N (0.02%) against calc. (wt.%): C (15.13%), H (1.27%), N(0%). For FcPW, CHN analysis shows obs. (wt.%): C (10.72%), H (0.40%), N (0.1%) against calc. (wt.%): C (10.5%), H (0.88%), N(0%). This indicates that the  $(\text{C}_5\text{H}_5)_2$  moiety is intact in the

hybrids. Further, ICP-OES analysis revealed mole ratio of Fe:Mo as 1:4 [wt.% values for Fe (obs. 7.40%, calc. 7.04%); Mo (obs. 50.6%, calc. 48.4%)] and that of Fe:W as 1:3.7 [wt.% values for Fe (obs. 5.07%, calc. 4.88%); W (obs. 62.6%, calc. 64.2%)]. The BET isotherm reveals textural features of the hybrid materials, tabulated in Table S1 in the ESI. The pore size and pore volume were found to be quite low for the hybrids. This is expected as polyoxometalates have low surface area  $< 10 \text{ m}^2/\text{g}$ .<sup>50</sup> Hence, the hybrid materials can be used as underlay materials before coating by paints so as to prevent permeation of moisture through the paint coating to the metal. In this manner, these can also replace the chromate conversion coatings.<sup>5,9</sup>

Thermogravimetric analyses were conducted as shown in Fig. 8. There are three weight loss steps in the case of hybrids FcPW and FcPMo, whereas in case of precursor, ferrocene, there is only one major weight loss step. The 1.8% and 10.2% weight losses observed for FcPW and FcPMo hybrid materials, respectively, up to 250°C and 380°C are due to loss of water molecules of crystallization and those present in the lattice. The second weight loss (8.9% at 250–470°C in FcPMo and 5.2% at 380–600°C in FcPW) is due to the decomposition of  $[\text{Fe}(\text{C}_5\text{H}_5)_2]^+$ .<sup>11</sup> Ferrocene undergoes sublimation around 100°C, and decomposes into Fe,  $\text{H}_2$  and other hydrocarbons around 400°C. The third and final weight loss about 21.1% beyond 490°C in FcPMo and about 4.6% beyond 600°C in FcPW are due to structural collapse of the polyanion.<sup>11,44</sup> These weight losses confirm the presence of ferrocenium cation and polyoxometalate anion in the hybrid materials. From TGA plots, the molecular formulae for the hybrids FcPMo and FcPW can be predicted, respectively, as  $[\text{Fe}(\text{C}_5\text{H}_5)_2]_3[\text{PMo}_{12}\text{O}_{40}] \cdot (\text{H}_2\text{O})_6$  and  $[\text{Fe}(\text{C}_5\text{H}_5)_2]_3[\text{PW}_{12}\text{O}_{40}] \cdot (\text{H}_2\text{O})_4$ .

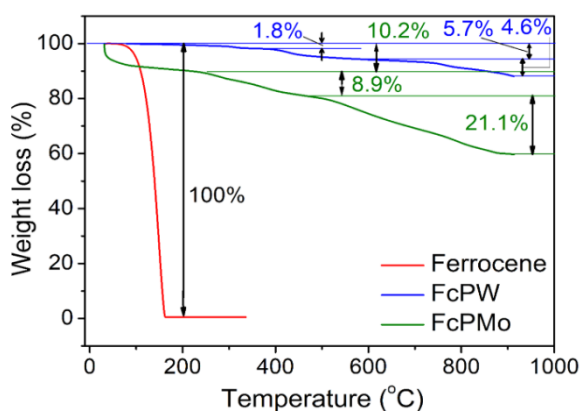


Figure 8 TGA profiles of ferrocene, FcPMo, and FcPW.

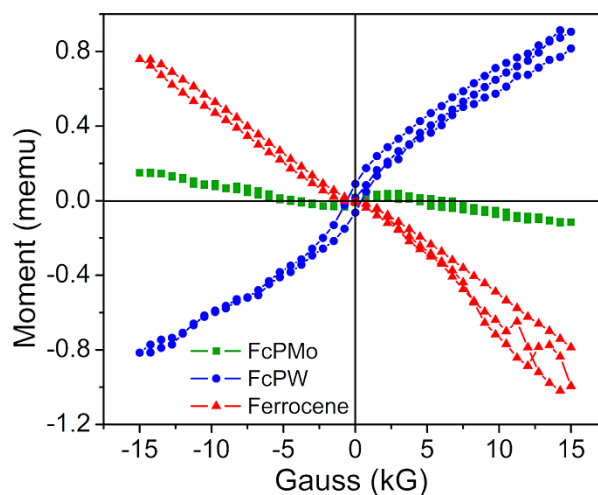
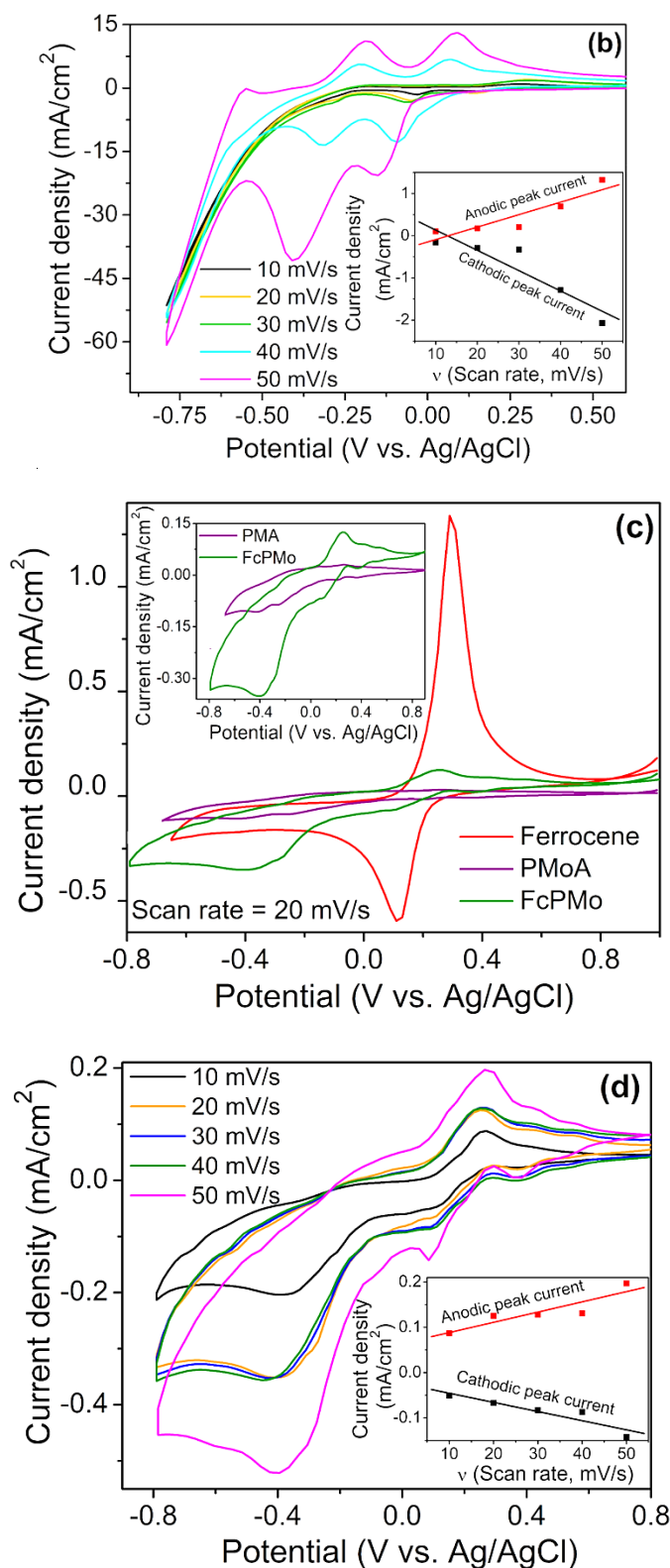
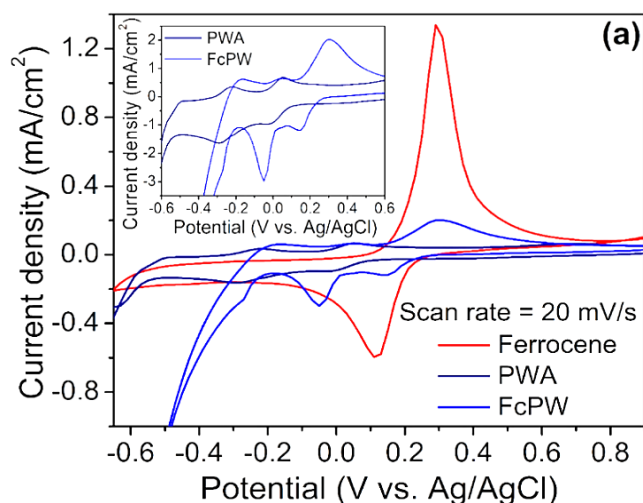


Figure 9 Vibrating sample magnetometer (VSM) curve of ferrocene, FcPMo and FcPW at room temperature.

Magnetization hysteresis curves were also recorded for ferrocene, FcPW and FcPMo as shown in Fig. 9. The measurements were done in an applied magnetic field at room temperature, with the field being swept from  $-15,000$  to  $+15,000$  gauss. It can clearly be seen that the hysteresis loop for all the samples is reversible. Ferrocene is diamagnetic in nature as reported in literature.<sup>32,51</sup> In the hybrid molecular material FcPW, however, the diamagnetic nature of ferrocene becomes predominantly paramagnetic. In the case of FcPMo, the diamagnetic nature of ferrocene is significantly diminished with a small percentage of paramagnetic behavior. The hysteresis loop reached saturation at the maximum applied magnetic field, with magnetic saturation values of  $-1$  memu,  $-0.12$  memu and  $0.93$  memu at room temperature for ferrocene, FcPW and FcPMo, respectively. In ferrocene,  $\text{Fe}(\text{C}_5\text{H}_5)_2$ , Fe is in +2 oxidation state, and the six electrons in  $3d$  orbital of  $\text{Fe}^{2+}$  pair up, thus making the complex diamagnetic in nature. However, an additional electron in  $[\text{Fe}(\text{C}_5\text{H}_5)_2]^+$  remains unpaired and causes the structure to be paramagnetic in nature.<sup>51</sup> For FcPW, there is predominant paramagnetic nature observed as W (+6) is reduced to W(+5), where an unpaired electron is present in  $5d$  orbital.<sup>16</sup> In the case of FcPMo, although the diamagnetic behaviour of ferrocene is significantly diminished, but the material is weakly paramagnetic. This could be attributed paramagnetic effect of  $\text{Fe}^{3+}$  being offset by weak paramagnetic effect of reduced species Mo(+5) having unpaired electron in a  $4d$  orbital, which is comparatively more tightly held by the nucleus. Another reason for weaker paramagnetism in Mo(+5) species could be due to equilibrium between paramagnetic and diamagnetic species as a result of formation of oxobridges.<sup>52</sup>



Cyclic voltammograms (CVs) of the samples ferrocene, FcPW, PWA, FcPMo and PMoA were recorded as shown in Fig. 10(a and c) with working electrode as glassy carbon (GC) coated *via* drop-casting with 20  $\mu\text{L}$  FcPMo/FcPW ink (10 mg of material in 200  $\mu\text{L}$  of 5% Nafion as binder + 300  $\mu\text{L}$  ethanol + 1000  $\mu\text{L}$  demineralized water); a counter electrode involving a Pt strip connected to Cu wire; and a Ag/AgCl reference electrode in sat. KCl; with 0.5 M  $\text{H}_2\text{SO}_4$  as electrolyte. The CVs of FcPW and FcPMo were recorded at different scan rates as shown in Fig. 10(b) and (d). We can observe distinct reversible redox steps for FcPW and PWA ( $\text{W}^{6+} \rightleftharpoons \text{W}^{5+}$  and  $\text{Fe}^{2+} \rightleftharpoons \text{Fe}^{3+}$ ) as shown in Fig. 10(a) and (b) which are characteristic of the precursors PWA and ferrocene. Similarly, for FcPMo and PMoA ( $\text{Mo}^{6+} \rightleftharpoons \text{Mo}^{5+}$  and  $\text{Fe}^{2+} \rightleftharpoons \text{Fe}^{3+}$ ) as shown in Fig. 10(c) and (d), distinct redox peaks are observed.<sup>19</sup> Further, as shown in the insets of Fig. 10(a) and (c), the redox peaks of both FcPW and FcPMo are shifting towards higher positive potential values when compared with peaks of PWA and PMoA, respectively. This indicates faster rate of reaction in forward sweep than in the reverse sweep. However, overall increased peak current densities in both FcPW and FcPMo indicate faster electrokinetics both in forward and reverse reactions in the electrocatalytic process. Also, the plot of current density vs. scan rate is plotted in the inset of Figs. 10(b, d) for FcPW and FcPMo redox systems. The ratio of  $i_{p,c}/i_{p,a}$  comes close to 1 for FcPW, while it is around 0.5 for FcPMo, which indicates that the redox process is reversible for FcPW. The linear relationship in both cathodic and anodic peak currents of FcPW and FcPMo with scan rate indicates that the redox process involves surface adsorbed electron transfer.



**Figure 10** CV plots for (a) ferrocene, FcPW and PWA; (b) FcPW at different scan rates; (c) ferrocene, FcPMo and PMoA; and (d) FcPMo at different scan rates.

### Corrosion inhibition study on stainless steel (316 grade)

Among the different methods adopted for corrosion studies, the most commonly used methods are weight loss method, EIS and potentiodynamic polarization studies. The corrosion rate obtained from weight loss studies is an integrated value of corrosion rate obtained over a period of time, and gives the total corrosion rate. However, the corrosion rate from impedance and potentiodynamic polarization studies give instantaneous values of corrosion rate at a specific time.<sup>53</sup> By using the Tafel extrapolation method on the polarization curves obtained in potentiodynamic studies,  $E_{\text{corr}}$ ,  $i_{\text{corr}}$  values are obtained. And by applying Stern-Geary equation, the polarization resistance ( $R_p$ ) is estimated. In absence of mass transport process, the polarization resistance ( $R_p$ ) is same as the charge transfer resistance ( $R_{\text{CT}}$ ). However, during corrosion, three processes, diffusion, adsorption and charge transfer controlled processes can occur at the electrochemical interface between electronic and ionic phases. This interface slows down the corrosion process. Now,  $R_p = R_{\text{CT}} + R_F$  for process involving adsorbed intermediate, where  $R_F$  is the resistance due to ionic pathways. Also,  $R_p = R_{\text{CT}} + R_D$  and  $(R_{\text{CT}} + W) \gg R_S$  for diffusion controlled process, where  $R_D$  is the diffusional impedance and is equal to Warburg impedance ( $W$ ) at sufficiently low frequency values.<sup>54</sup> In potentiodynamic polarization method, the effects of capacitance associated with adsorbed intermediate ( $C_f$ ), electrical double layer capacitance due to constant phase element ( $Q_{\text{dl}}$ ), solution resistance ( $R_S$ ), charge transfer resistance ( $R_{\text{CT}}$ ), resistance due to ionic pathways ( $R_f$ ) on corrosion rate are not taken into account. The influence of these factors on corrosion rate can be addressed by using electrochemical impedance spectroscopy (EIS). In this method, an equivalent electrical circuit is used to represent the electrochemical surface of the electrode during corrosion process using circuit parameters ( $C_f$ ,  $R_S$ ,  $R_{\text{CT}}$ ,  $Q_{\text{dl}}$ ,  $R_f$ ). Hence, instantaneous corrosion rate can be determined from potentiodynamic polarization curves using Tafel extrapolation method, and the result can be validated by instantaneous corrosion rate from EIS and total corrosion rate from weight loss method.

From the weight-loss method, the corrosion rate (in mmy) of the steel plates coated with FcPW and FcPMo hybrid materials is calculated as

$$R = \frac{\text{weight loss} \times 8.75 \times 10^4}{d \times A \times t}$$

where Wt. loss is weight loss in g,  $d$  is the density of stainless steel in  $\text{g/cm}^3$ ,  $A$  is exposed area of the electrode in  $\text{cm}^2$ , and  $t$  is the exposure time in hours. The inhibition efficiency  $\eta\%$  and the



degree of surface coverage  $\theta$  are calculated from the following equations.<sup>7,14,55</sup>

$$\eta\% = \frac{R_{\text{corr}}^0 - R_{\text{corr}}}{R_{\text{corr}}^0} \times 100$$

$$\theta = \frac{R_{\text{corr}}^0 - R_{\text{corr}}}{R_{\text{corr}}^0}$$

where  $R_{\text{corr}}^0$  and  $R_{\text{corr}}$  are the corrosion rates of bare steel and steel coated with hybrid material, respectively. After immersing in 0.5 M  $\text{H}_2\text{SO}_4$  for 24 h, the weight loss measurements were obtained as shown in Table 1.

**Table 1** Corrosion rate and inhibition efficiency by weight loss method

Material	$R$ (mmy)	$\eta$ (%)	$\theta$	Bare and coated steel plates immersed in 0.5 M $\text{H}_2\text{SO}_4$ for 24 h
Bare steel (SS) (316 grade)	15.15	-	-	
SS@ FcPW	0.14	99.1	0.991	
SS@ FcPMo	0.092	99.4	0.994	

The AC perturbation was applied before the potentiodynamic test during EIS recording where known amplitude (5 mV for SS@FcPW and SS@FcPMo and bare steel) was applied in the frequency range 100 kHz to 0.01 Hz. This is because during potentiodynamic polarization measurement, corrosion process will take place. Thus, the error due to impedance measurement on corroded sample can be avoided. EIS of the bare steel plate and that of steel plate coated with FcPW and FcPMo were recorded with 85%  $iR$  correction, and Nyquist plots were plotted. In the Nyquist plot shown in Fig. 11(a) for the coated electrodes (SS@FcPW and SS@FcPMo), the first part of semicircle at higher characteristic frequency ( $\omega$ ) is due to the coated surface. The second incomplete part of the semicircle at

lower characteristic frequency is due to formation of oxide layer/solution interface during corrosion.<sup>56</sup> Hence, in bare steel the  $\omega_{\max}$  value is higher as compared to SS@FcPW and SS@FcPMo, indicating corrosion inhibition by the hybrid materials. The equivalent electrical circuit is shown in Fig. 11(a) inset fits the EIS data of SS, SS@FcPW and SS@FcPMo. Here,  $R_s$  is the solution resistance,  $R_f$  is the resistance due to the ionic pathways passing through the passive layer,  $C_f$  is the capacitance of the passive film formed on the surface of electrode,  $Q$  (replaces  $C$  dispersion effect caused by roughness of the electrode interface<sup>57</sup>) is the constant phase angle element representing electric double-layer capacitance,  $R_{CT}$  is the charge transfer resistance and  $W$  is the Warburg impedance. The validity of the steady state EIS data is confirmed using Kramers-Kronig (KK) transformation. This is done by fitting model  $[-R - (RC)_m]$  having series connection of  $m$  number of resistors and capacitors connected in parallel, and  $m$  is the no. of complex plane data points in the spectrum.<sup>58,59</sup> Using ZSimpWin software, KK analysis is applied and the Nyquist plot is extrapolated for bare steel, SS@FcPW and SS@FcPMo to obtain  $\chi^2$  values as shown in Fig. 11(a).

Comparing the Nyquist plots as shown in Fig. 11(a) and parameters obtained after fitting as shown in Table 2, we can calculate the corrosion inhibition efficiency as per the following equation.<sup>7,14,55</sup>

$$\eta\% = \frac{R_{CT} - R_{CT}^0}{R_{CT}} \times 100$$

It is found that SS@FcPW shows 65% and SS@FcPMo shows 74% corrosion inhibition efficiency.

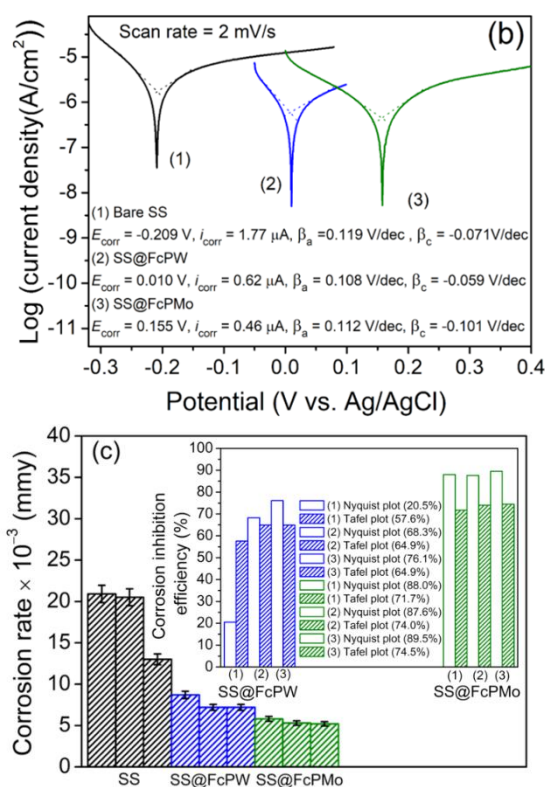
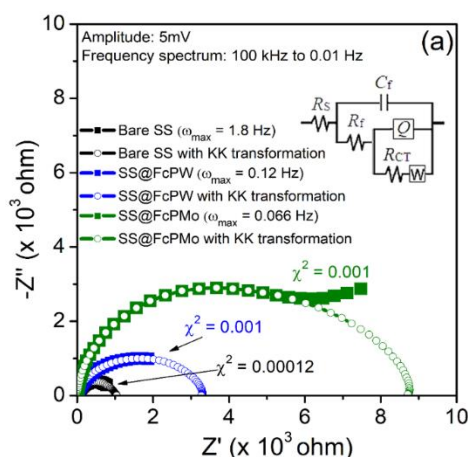


**Figure 11** (a) Nyquist plots of bare steel, FcPMo, FcPW with KK transformation and characteristic frequencies ( $\omega_{\max}$ ). (b) Tafel plots of bare steel, FcPMo, FcPW. (c) Reproducibility tests with error bars (Fig. 11c is corrected, but the inset of the figure 11c has no change).

**Table 2** Parameters obtained from EIS

Electrode	$R_s$ (ohm cm <sup>2</sup> )	$C_f$ (μF/cm <sup>2</sup> )	$R_f$ (ohm cm <sup>2</sup> )	$Q_{dl}$ (μF/cm <sup>2</sup> )	$R_{CT}$ (ohm cm <sup>2</sup> )
Bare Steel	1.8	47.3	4.4	164.8	1040.0
(SS)					
(316 grade)					
SS@FcPW	2.3	85.8	25.3	259.8	3285.0
SS@FcPMo	3.5	82.8	39.4	128.8	8375.0

Tafel plots from the bare steel plate and that of steel plate coated with FcPW and FcPMo are plotted from potentiodynamic studies done with 85%  $iR$  correction (Fig. 11b). The potentiodynamic polarization studies are generally conducted at low scan rate.<sup>60,61</sup> This is because of the charging current density varies linearly with the product of scan rate and double layer capacitance ( $Q_{dl}$ ). Now, due to the interdependence of  $Q_{dl}$  on the electrode potential, it is difficult to isolate the charging current density from the external current density. This causes the potentiodynamic polarization curve to be distorted in the region close to  $E_{corr}$  when faradaic current

density is low. In a wide potential range, this distortion leads to erroneous values for Tafel slopes and  $i_{\text{corr}}$ . The extent of this distortion depends upon the scan rate chosen for the potentiodynamic measurement. Using higher scan rates causes reduction in diffusion layer, as a result of which higher charging current density corresponding to an applied potential is observed.<sup>62</sup> In contrast, choosing low scan rates will reduce the disturbance caused by charging current density. Thus, the distortion in the potentiodynamic polarization curve is almost negligible. However, in highly conducting electrolytes, the shifts observed in the polarization plots can be very small. Also in the presence of highly active metals or catalytic surfaces, higher scan rates can be chosen to obtain limiting anodic or cathodic current response, as low scan rates can give noise. The experiments were conducted at different scan rates (1, 2, 3, 4, 5, 10 mV/s). The scan rate 2 mV/s gave the best result among these, so the Tafel plots corresponding to 2 mV/s are shown in Fig. 11(b). For ideal inhibitors, the  $E_{\text{corr}}$  values shift to more negative side as they block the cathodic sites. However, in SS@FcPW and SS@FcPMo the  $E_{\text{corr}}$  values are moving towards more positive side, indicating mixed type of corrosion inhibition. These inhibitors can block both cathodic and anodic sites, thus reducing the corrosion rate. Inhibition efficiency is calculated as:<sup>7,14,55</sup>

$$\eta\% = \frac{i_{\text{corr}}^0 - i_{\text{corr}}}{i_{\text{corr}}^0} \times 100$$

Calculations from Tafel plots using Tafel extrapolation technique are done to obtain the percentage corrosion inhibition and

corrosion rate (measured in millimeter per year).<sup>63</sup> The results are given in Table 3. The corrosion inhibition efficiency for SS@FcPW is 64% and that of SS@FcPMo is 75%. Polarization resistance ( $R_p$ ) can also be calculated from the Tafel plots by Stern Geary equation:<sup>64</sup>

$$-i_{\text{corr}} = \frac{B}{R_p} \text{ where } B = \frac{\beta_a \beta_c}{2.3(\beta_a + \beta_c)}$$

$$\log R_p = \log B - \log i_{\text{corr}}$$

The Tafel slope values ( $\beta_a$  and  $\beta_c$ ) are obtained by Tafel extrapolation technique. In this method, the linear portion of the anodic and cathodic curves in the Tafel plot are fit linearly using Origin 7.0. The  $R_p$  and corrosion rate values are estimated using the slope values obtained from the linear fit and compared with the values obtained by curve fitting using the CH Instrument software (Table 3). We have then considered the values obtained from the Tafel extrapolation technique. Accordingly, the values of  $R_p$  are 8995 ohm cm<sup>2</sup> for bare steel, 26722 ohm cm<sup>2</sup> for SS@FcPW, 37194 ohm cm<sup>2</sup> for SS@FcPMo. This confirms significant corrosion inhibition of the steel plates coated with the hybrid materials.

The corrosion test experiments are repeated using three similar working electrodes each for bare steel, SS@FcPW and SS@FcPM. The Nyquist and Tafel plots of the repeated experiments are given in Fig. S4 (ESI). Figure 11(c) and Table S2 (ESI) show the results obtained from the replicate experiments with corresponding error values.

**Table 3** Calculations from Tafel plots using Tafel extrapolation technique

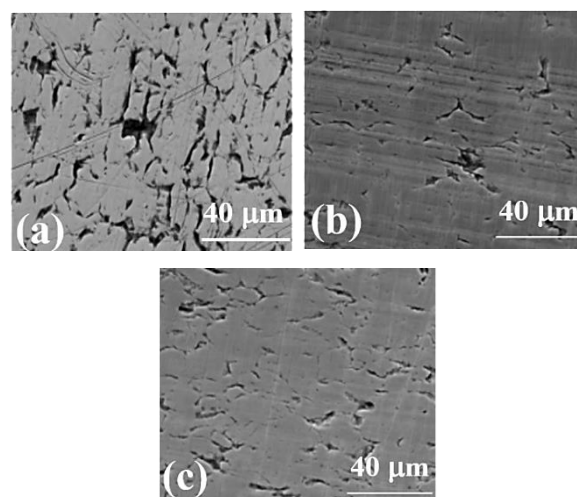
Electrode	Method	$E_{\text{corr}}$ (V)	$i_{\text{corr}}$ ( $\mu\text{A}/\text{cm}^2$ )	Corrosion inhibition $\eta$ and corrosion rate	$\beta_a$ (V $\text{dec}^{-1}$ )	$\beta_c$ (V $\text{dec}^{-1}$ )	$R_p$ (ohm $\text{cm}^2$ )
Bare Steel (SS) (316 grade)	#Instr.	-0.210	2.10	Corrosion rate $= \frac{i_{\text{corr}} \times M}{n \times F \times d} = \frac{21.0 \times 10^{-7} \times 56}{2 \times 96500 \times 7.87} = 7.74 \times 10^{-11} \text{ cm/s} = 0.024 \text{ mmy}$	0.125	-0.068	8804
	*Calc.	-0.210	1.77	Corrosion rate $= 6.52 \times 10^{-11} \text{ cm/s} = 0.021 \text{ mmy}$	0.119	-0.053	8995
SS@ FcPW	Instr.	0.0100	0.62	$\eta = \frac{i_{\text{corr,steel}} - i_{\text{corr,FcPW}}}{i_{\text{corr,steel}}} = \frac{(17.7 - 6.2) \times 10^{-7} \times 10^2}{17.7 \times 10^{-7}} = 64.9\%$ Corrosion rate $= 2.28 \times 10^{-11} \text{ cm/s} = 0.0072 \text{ mmy}$	0.102	-0.059	26222
	Calc.	0.0100	0.62	$\eta = 64.9\%$ Corrosion rate $= 2.28 \times 10^{-11} \text{ cm/s} = 0.0072 \text{ mmy}$	0.108	-0.059	26722
SS@ FcPMo	Instr.	0.0155	0.56	$\eta = 68.3\%$ Corrosion rate $= 2.06 \times 10^{-11} \text{ cm/s} = 0.0065 \text{ mmy}$	0.084	-0.088	33344
	Calc.	0.0155	0.46	$\eta = 74.0\%$ Corrosion rate $= 1.69 \times 10^{-11} \text{ cm/s} = 0.0053 \text{ mmy}$	0.112	-0.101	37194

#Instr. From CH Instrument software

\*Calc. From Tafel extrapolation method

mmy denotes millimetre per year ( $\text{mm year}^{-1}$ )

Inspection of corroded stainless steel plates after immersion in 0.5 M  $\text{H}_2\text{SO}_4$  for 3 h using SEM (Fig. 12) confirms that the formation of corrosion cracks is reduced when the stainless steel plates were coated with FcPMo and FcPW. The corroded steel plates were analyzed by AFM after immersion in 0.5 M  $\text{H}_2\text{SO}_4$  for 24 h. Figure 13 shows the AFM images and the depth analyses for each of the substrates coated on stainless steel plate. As expected, both the surface roughness and depth of the crack are large for SS, smaller for SS@FcPW and least for SS@FcPMo.

**Figure 12** SEM images of corroded (a) bare SS plate, (b) SS coated with FcPMo; and (c) SS coated with FcPW.



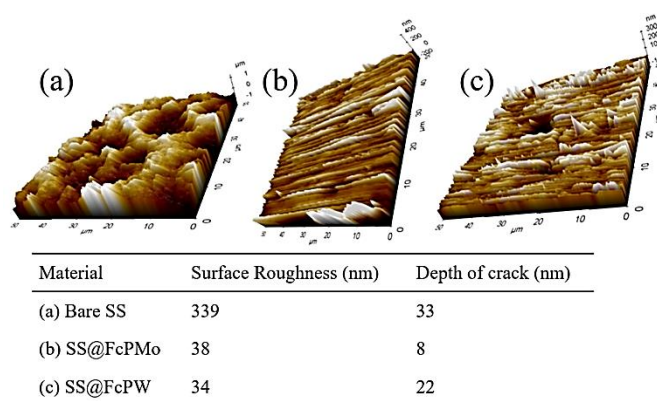


**Figure 13** AFM images of uniform corrosion observed in SS plate: (a) bare steel; (b) SS@FcPMo; and (c) SS@FcPW.

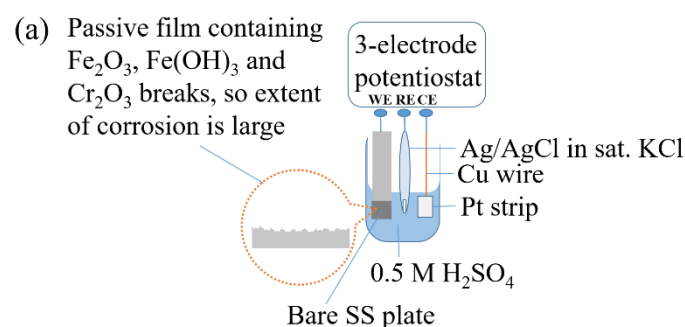
In an extended study, the corrosion studies were performed using simulated body fluid (pH = 7.5) using Ringer's solution (containing 8.6 g NaCl, 0.3 g KCl, 0.33 g CaCl<sub>2</sub> in 1000 mL deionized H<sub>2</sub>O) maintaining the temperature at 37°C.<sup>65,66</sup> Weight loss measurements were done for the bare stainless steel plate and stainless steel coated with the hybrid materials immersed in Ringer's solution for a period of 24 h. The corrosion inhibition efficiency was computed based on the weight loss of the corroded plated, and was found as SS@FcPW (72.1%) and SS@FcPMo (95.6%). EIS was recorded in the frequency range 100 kHz to 0.01 Hz at OCP and 5 mV amplitude. The parameters obtained from Nyquist plots are shown in Table S3 (ESI). The inhibition efficiency shown by SS@FcPW and SS@FcPMo are 54.4% and 77.2%, respectively. Finally, polarization studies for Tafel plots were performed from -200 to +200 mV with respect to OCP at different scan rates (1, 2, 3, 4, 5, 10 mV/s). The plots and results considering scan rate of 2 mV/s are shown in Fig. S5 and Table S4 of ESI. The values were obtained both by experimental curve fitting from instrument's software and manual calculations from linear fitting in Tafel extrapolation method. As the calculated values were considered more accurate, these are shown in Table S4. SS@FcPW showed an efficiency of 32.3%, while SS@FcPMo showed 71.2%. The corrosion test experiments are repeated using three similar working electrodes each for bare steel, SS@FcPW and SS@FcPM. The Nyquist and Tafel plots of the repeated experiments are given in Fig. S6 (ESI). Figure S6(C) and Table S5 show the results obtained from the replicate experiments with corresponding error values.

The parent polyoxometalate is stable in solution of pH 2 to 3, however, as the pH increases, lacunary polyoxometalate anion is formed due to loss of an addenda atom (M = W, Mo, etc.) and vacancies are created. Monolacunary Keggin anions can result from

the parent polyoxometalate by addition of base.<sup>20,67,68</sup> Similarly, di- and trilacunary anions are formed at higher pH values by increasing the concentration of base. For instance, the lacunary polyoxometalate [PW<sub>11</sub>O<sub>39</sub>]<sup>7-</sup> can be stable up to pH = 7.5, beyond which, complete decomposition of Keggin anion into constituents P<sub>2</sub>O<sub>5</sub> and WO<sub>3</sub> (or MoO<sub>3</sub>) takes place.<sup>20,68</sup> The corrosion rates and corrosion inhibition efficiencies calculated from Tafel extrapolation method are as follows: bare SS (0.036 mmy); SS@FcPW (0.025 mmy, 32%); SS@FcPMo (0.011 mmy, 71%). The values for  $R_p$  are as follows: bare steel = 7709 ohm cm<sup>2</sup>, SS@FcPW = 11070 ohm cm<sup>2</sup>, SS@FcPMo = 30993 ohm cm<sup>2</sup>.

### Mechanism of corrosion inhibition

It is known that Mo is present in the stainless steel (SS316) as a corrosion inhibitor, especially of crevice corrosion.<sup>5</sup> However, it is interesting to see how the coating of hybrid materials FcPW and FcPMo prevents uniform corrosion by interacting with the stainless steel plate. As mentioned earlier, the shifting of  $E_{\text{corr}}$  values to positive side indicate mixed type of corrosion inhibition. The anodic site is blocked due to redox activity of Fe<sup>3+</sup> present in ferrocenium ion which inhibits the dissolution of iron as  $\text{Fe(s)} \rightarrow \text{Fe}^{2+}(\text{aq}) + 2e^-$ . The cathodic sites are blocked by stabilization of oxide film over the electrode surface due to strong oxidizing nature of polyoxometalate. This stable film prevents diffusion of electrolyte to the steel surface, thus inhibiting the cathodic reaction  $[2\text{H}^+(\text{aq}) + 2e^- \rightarrow \text{H}_2(\text{g})]$ . The possible mechanism for corrosion inhibition by hybrid materials is presented in Fig. 14.



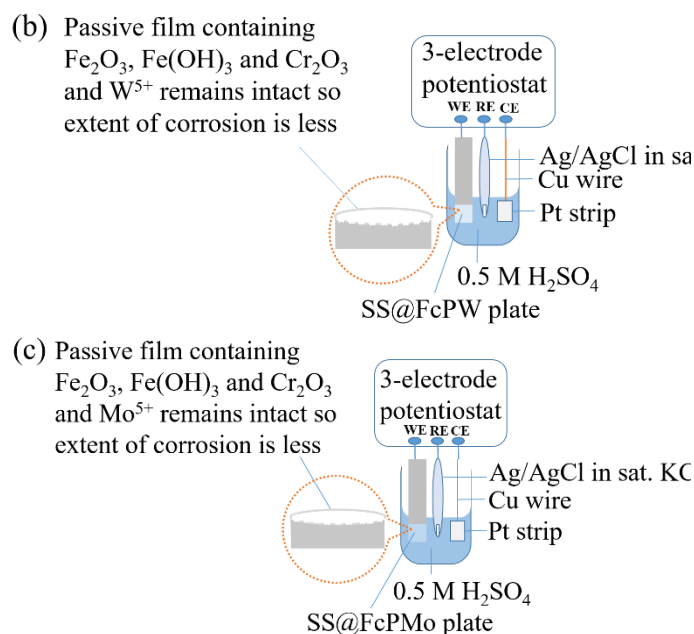


**Figure 14** The corrosion mechanism in (a) bare SS, (b) SS@FcPW; and (c) SS@FcPMo plates.

For bare steel plate (SS316), just after a few minutes, the passive film composed of  $\text{Fe}_2\text{O}_3$ ,  $\text{Fe}(\text{OH})_3$  and  $\text{Cr}_2\text{O}_3$  breaks down and corrosion starts. Hence, a large extent of corrosion is observed within a short period of time. On the contrary, for both SS@FcPW and SS@FcPMo plates, even after 24 h, the passive film composed of  $\text{Fe}_2\text{O}_3$ ,  $\text{Fe}(\text{OH})_3$  and  $\text{Cr}_2\text{O}_3$  remains intact due to protection offered by  $[\text{PW}_{12}\text{O}_{40}]^{3-}$  or  $[\text{PMo}_{12}\text{O}_{40}]^{3-}$  and  $\text{Fe}^{3+}$  oxidizing

species. The  $\text{Fe}^{3+}$  ion present as  $[\text{Fe}(\text{C}_5\text{H}_5)_2]^+$  in FcPW or

FcPMo, undergoes reduction reaction and gets converted to  $\text{Fe}^{2+}$ , thus inhibiting the dissolution of  $\text{Fe}(\text{s})$  in the anode ( $\text{Fe}(\text{s}) \rightarrow \text{Fe}^{2+}(\text{aq}) + 2e^-$ ) by means of Le Chatelier's principle. In the case of SS@FcPW, due to the presence of POM anions,  $\text{W}^{6+}$  is reduced to  $\text{W}^{5+}$  and gets incorporated in the film, thus inhibiting corrosion.<sup>20</sup> While in the case of SS@FcPMo,  $\text{Mo}^{6+}$  is reduced to  $\text{Mo}^{5+}$  and gets incorporated in the film, thus inhibiting corrosion further.<sup>9,20</sup> As Mo is a better corrosion inhibitor than W, thus the presence of  $\text{Mo}^{5+}$  in the film helps reduce the extent of corrosion even further. This concurs with the higher corrosion inhibition efficiency obtained for SS@FcPMo plates over SS@FcPW plates by EIS and Tafel studies.

### Optimized structure and frontier molecular orbitals of inhibitor materials

Based on the experimental results discussed earlier, the molecular structure of the inhibitors is modelled and the energy minimised structure of the inhibitor materials FcPW and FcPMo are shown in Figs. 15(a) and (b).

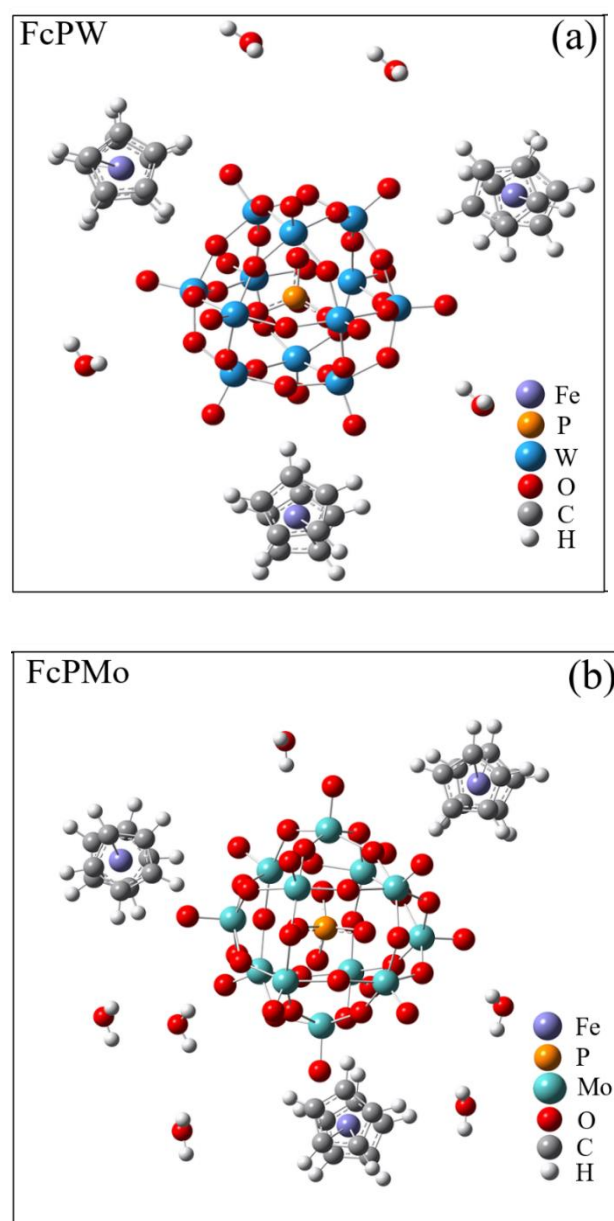


**Figure 15.** The optimized structures of the inhibitor materials (a) FcPW and (b) FcPMo.

The bond lengths, bond angles and torsion angles from the optimized structures of the inhibitors FcPW and FcPMo are presented in Tables S6-S11. From Tables S6 and S7, it is seen that the lengths of C–C bonds in cyclopentadienyl ring and Fe–C bonds are in the range of 1.42–1.44 Å and 2.03–2.12 Å, respectively. Thus, in the hybrid materials FcPW and FcPMo, the bond distances of C–C and Fe–C

are slightly increased compared to ferrocene, where C–C and Fe–C bond lengths are of the order of 1.41 Å and 2.0 Å. This slight elongation is attributed to the formation of  $[\text{Fe}(\text{C}_5\text{H}_5)_2]^+$ .<sup>69</sup> In Keggin polyoxometalate,  $[\text{PW}_{12}\text{O}_{40}]^{3-}$ , the bond lengths are 1.7 Å for W–O<sub>c</sub>, 1.9 Å for W–O<sub>t</sub>, 2.43 Å for W–O<sub>b</sub>–W and 1.5 Å for P–O.<sup>70,71</sup> However, in FcPW, they are found to be 1.71–1.96 Å for W–O, 2.46–2.49 Å for W–O<sub>b</sub>–W and 1.55 Å for P–O (Table S6, ESI). Thus, there is slight elongation in the W–O<sub>c</sub>, W–O<sub>t</sub> and W–O–W bonds due to interaction with ferrocenium cation, causing a shift in electron density. In  $[\text{PMo}_{12}\text{O}_{40}]^{3-}$ , the bond lengths reported are 1.7 Å for Mo–O<sub>c</sub>, 1.95 Å for Mo–O<sub>t</sub> and 2.45 Å for Mo–O<sub>b</sub>–Mo, and 1.55 Å for P–O.<sup>41,71</sup> The corresponding bond lengths in FcPMo are found from Table S7 (ESI) as 1.68–2.00 Å for Mo–O, 2.38–2.51 Å for Mo–O<sub>b</sub>–Mo and 1.55 Å for P–O. Hence, there is slight difference in Mo–O<sub>c</sub>, Mo–O<sub>t</sub> and Mo–O–Mo bonds are due to the interaction with ferrocenium cation, causing a shift in electron density.

Another aspect to be looked upon for ensuring strong adsorption on the iron surface of stainless steel plate is the planar structure of an inhibitor molecule. For this purpose, all the bond angles and torsion angles of FcPMo and FcPW are analyzed. The bond angles are given in Tables S8 and S9, and it is observed that most of the bond angles for the cyclopentadienyl ring in FcPW and FcPMo lie close to 120° (highlighted in grey). This shows that C atoms of cyclopentadienyl ring atoms are  $sp^2$  hybridized, thereby indicating a planar orientation. Also, the  $[\text{PW}_{12}\text{O}_{40}]^{3-}$  and  $[\text{PMo}_{12}\text{O}_{40}]^{3-}$  are partially planar as the bond angles range from 68° to 160°, with some lying close to 120° (highlighted in grey). Therefore, the inhibitor molecule has partly planar structure.

Now, we have to confirm whether both the cyclopentadienyl ring and polyoxometalate structure take part in adsorption on the iron surface, or whether one participates in adsorption while the other remains free. For this purpose, we need to look at the torsion angles listed in Tables S10 and S11. The torsional angles formed by the planes of atoms (highlighted in orange) in both FcPW and FcPMo lie near to either 0 or 180°. This confirms that the orientation of the cyclopentadienyl ring and polyoxometalate structure are somewhat planar with respect to each other. Hence, they do not completely lie in different planes. This observation reveals that to some extent both the moieties participate in the adsorption. This is further validated by the fact that polyoxometalate acts as an oxidizing agent, by oxidizing the anodic reaction, while  $[\text{Fe}(\text{C}_5\text{H}_5)_2]/[\text{Fe}(\text{C}_5\text{H}_5)_2]^+$  redox couple aids in Fe(s) to  $\text{Fe}^{2+}$  oxidation.

Anodic reaction:  $\text{Fe(s)} \rightarrow \text{Fe}^{2+}(\text{aq}) + 2e^-$

Cathodic reaction:  $2\text{H}^+(\text{aq}) + 2e^- \rightarrow \text{H}_2(\text{g})$

The presence of heteroatom in the polyoxometalate ring further aids in adsorption of iron as has been the case in literature where heterocyclic rings are considered to be dominant in adsorption.<sup>55</sup> For further adsorption studies, the adsorption of the inhibitor onto the steel surface depends on the energy gap between the frontier molecular orbital energy level of the inhibitor molecule and the Fermi level of the Fe metal atom.<sup>55,72,73</sup> Both the frontier molecular orbitals of FcPW and FcPMo are shown in Fig. 16.

## ARTICLE

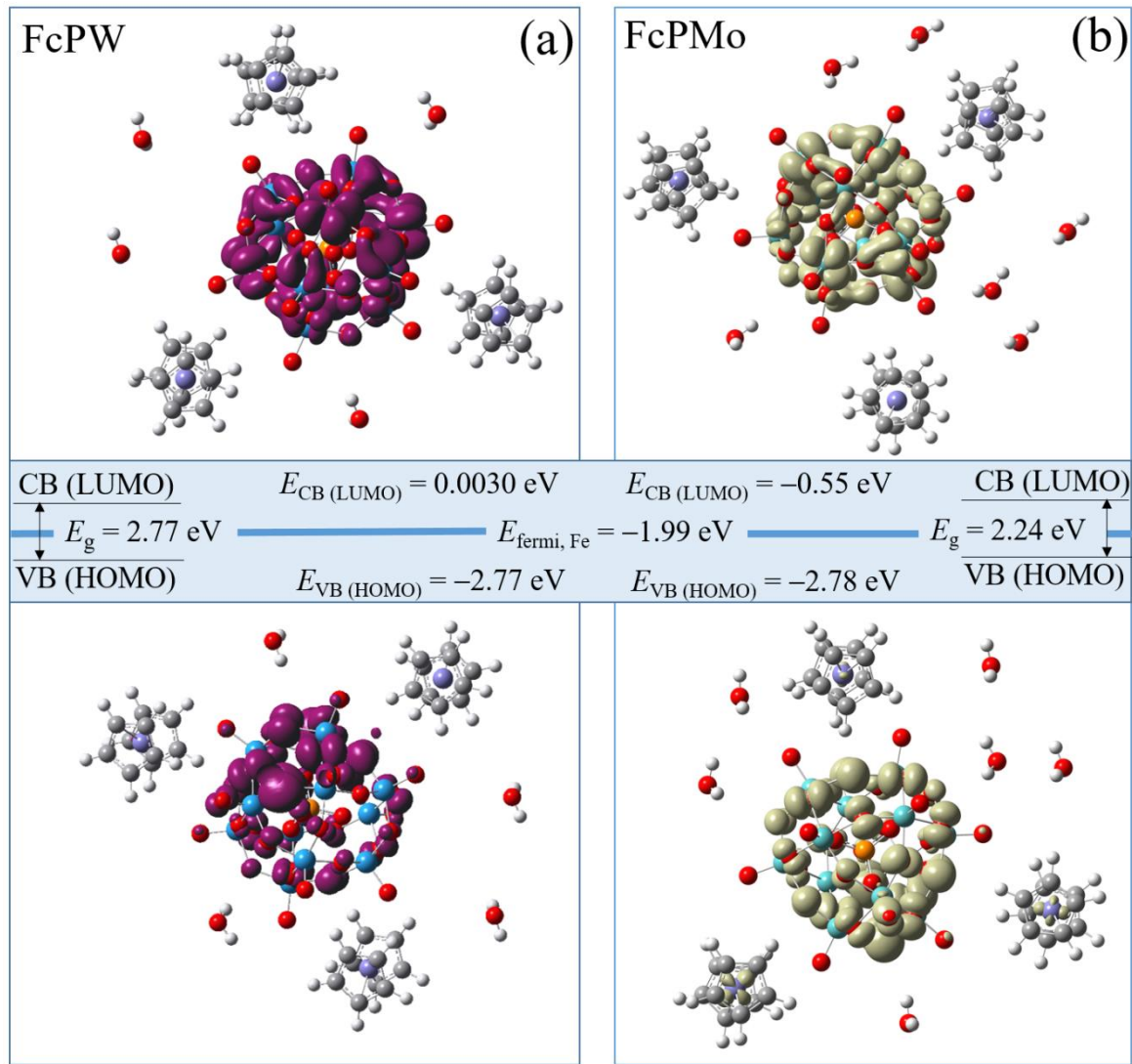


**Figure 16** The Fermi level of iron and frontier molecular orbitals (HOMO and LUMO) of (a) FcPW; and (b) FcPMo materials.

The Fermi level of iron and frontier orbital energies (eV) of inhibitors are also presented in the figure. In the figures, VB represents valence band, which is the highest occupied molecular orbital (HOMO) and CB represents conduction band, which is the lowest unoccupied molecular orbital (LUMO). Based on the first principle calculations, the HOMO level of single Fe(100) atom is at  $-1.9973 \text{ eV}$  and LUMO level is at  $3.0071 \text{ eV}$ . From Table 4, we have

$$\begin{aligned}
 & \left[ E_{VB(HOMO)_{Fe}} - E_{CB(LUMO)_{FcPW}} = -2.00 \text{ eV} \right] \\
 & \ll \left[ E_{VB(HOMO)_{FcPW}} - E_{CB(LUMO)_{Fe}} = -5.77 \text{ eV} \right] \\
 & \left[ E_{VB(HOMO)_{Fe}} - E_{CB(LUMO)_{FcPMo}} = -1.44 \text{ eV} \right] \\
 & \ll \left[ E_{VB(HOMO)_{FcPMo}} - E_{CB(LUMO)_{Fe}} = -5.78 \text{ eV} \right]
 \end{aligned}$$

**Table 4** Quantum mechanical parameters obtained from first principle studies

Inhibitor	$E_{\text{VB(HOMO)}} \text{ (eV)}$	$E_{\text{CB(LUMO)}} \text{ (eV)}$	$E_{\text{g}} \text{ (eV)}$	$I \text{ (eV)}$	$A \text{ (eV)}$	$\chi \text{ (eV)}$	$\eta \text{ (eV)}$	$\Delta n$
FcPW	−2.77	+0.003	2.77	2.77	−0.003	1.38	1.38	1.24
FcPMo	−2.78	−0.550	2.23	2.78	+0.550	1.66	1.11	1.42

Therefore, the energy gap between  $E_{\text{LUMO}}$  level of FcPW (or FcPMo) and  $E_{\text{Fermi, Fe}}$  is comparatively smaller than that of  $E_{\text{HOMO}}$  levels and  $E_{\text{Fermi, Fe}}$ . This indicates that electron transfer from the iron surface to the  $E_{\text{LUMO}}$  level of inhibitor is possible. Also, out of FcPW and FcPMo, the  $E_{\text{LUMO}}$  of FcPMo is closer to the Fermi level of iron. This concurs with the experimental observation of higher adsorption of FcPMo over the iron surface, thereby leading to higher corrosion inhibition efficiency. Further, quantum mechanical parameters for hybrid materials FcPW and FcPMo acting as inhibitors are derived from Koopman's theorem and Pearson's method.<sup>74</sup> As per Koopman's theorem, ionization potential  $[I = -E_{\text{VB(HOMO)}}]$  and electron affinity  $[A = -E_{\text{CB(LUMO)}}]$ . From these two parameters, absolute electronegativity  $[\chi = (I + A) / 2]$  and global hardness  $[\eta = (I - A) / 2]$  of a material can be obtained. From the Pearson method, we can predict the number of electrons being transferred from the inhibitor molecule to the Fe(110) surface using the expression  $[\Delta n = (\phi_{\text{Fe}} - \chi_{\text{inhibitor}}) / 2(\eta_{\text{Fe}} + \eta_{\text{inhibitor}})]$ , where  $\phi_{\text{Fe}}$  is the work function of Fe(110) which is 4.82 eV and  $\eta_{\text{Fe}} = 0$ .<sup>74,75</sup> All the parameters are calculated and listed in Table 4. From the table, the  $\Delta n$  values for FcPW and FcPMo are 1.24 and 1.42, respectively. These values indicate that the fraction of electrons is transferred from the inhibitor molecules FcPW and FcPMo to the vacant  $d$ -orbital of Fe metal on the surface of stainless steel plate. The fraction of electrons transferred in the case of SS@FcPMo is more than that of SS@FcPW. So, there is increased adsorption of the inhibitor molecule on the metal surface, and therefore enhanced corrosion inhibition of stainless steel in the case of SS@FcPMo.

## 4. Conclusions

The synthesis and molecular properties of charge transfer compounds  $[\text{Fe}(\text{C}_5\text{H}_5)_2]_3[\text{PW}_{12}\text{O}_{40}] \cdot (\text{H}_2\text{O})_4$  and  $[\text{Fe}(\text{C}_5\text{H}_5)_2]_3[\text{PMo}_{12}\text{O}_{40}] \cdot (\text{H}_2\text{O})_6$  are reported. The UV-Vis diffuse reflectance spectra show charge transfer bands at ca. 620 nm for FcPW and FcPMo, indicating the charge transfer between the phosphotungstate/phosphomolybdate anions and ferrocene. IR

analysis shows that the cationic and anionic moieties are intact in the molecular hybrid materials which are thermally more stable than ferrocene. Powder XRD patterns show that the hybrids possess layered-type structures. The VSM studies revealed that there is a change in magnetic behaviour from diamagnetism in ferrocene to predominant paramagnetism in the hybrid FcPW and highly diminished diamagnetism in FcPMo. These hybrid molecular materials show corrosion inhibition properties on stainless steel (316 grade) plates undergoing uniform corrosion in 0.5 M  $\text{H}_2\text{SO}_4$  solution as well as Ringer's solution, determined by weight loss method, impedance spectra and Tafel plots. The corrosion inhibition efficiencies for FcPW (weight loss: 99.1%; EIS: 68.3%; polarization studies: 64.9%) and for FcPMo (weight loss: 99.4%; EIS: 87.6%; polarization studies: 74.0%) in 0.5 M  $\text{H}_2\text{SO}_4$ . For extended study carried out for corrosion inhibition of stainless steel plates coated with the hybrid materials in Ringer's solution, the efficiencies are: FcPW (weight loss: 72.1%; EIS: 54.4%; polarization studies: 32.3%) and for FcPMo (weight loss: 95.6%; EIS: 77.2%; polarization studies: 71.2%). The  $E_{\text{corr}}$  values move from to more anodic values for the hybrid materials compared to bare steel, indicating mixed-type of corrosion inhibition. These results are supported by computational studies using frontier molecular orbitals, bond lengths and bond angles of the hybrid materials.

## Conflicts of interest

There are no conflicts to declare.

## Acknowledgements

DSEHC has been funded by the Department of Science and Technology, Government of India, through grant no. DST/TMD/SERI/HUB/1(C). Sruthi thanks IIT Madras for granting JRF and SRF fellowships. Shanmugam received the Institute Postdoctoral Fellowship of IIT Madras. SAIF and the High-Performance Computing Environment (HPCE) of IIT Madras were very helpful during the carrying out of this work.



## References

1. E. Bardal (Ed.) *Different Forms of Corrosion Classified on the Basis of Appearance in Corrosion and Protection*, Springer, London, 2004, p.89.
2. S.C. Dexter, in *Corrosion*, ASM International, Materials Park, OH, vol. 13, 1987, p. 80.
3. M.G. Fontana, *Corrosion Engineering*, 3rd ed., McGraw-Hill, NY, 1986, pp. 282-283.
4. B.D. Craig and D.B. Anderson (Eds.), *Handbook of Corrosion Data*, 2nd ed., ASM International, OH, 1995, pp. 366-375.
5. D.F. Williams, E.J.C. Kellarb, D.A. Jessona and J.F. Watts, *Appl. Surf. Sci.*, 2017, **403**, 240-247.
6. D. Tablot and J. Tablot, *Corrosion Science and Technology*, CRC Press, Boca Raton, 1998, pp. 226-282.
7. S.R. Gupta, P. Mourya, M.M. Singh and V.P. Singh, *J. Organomet. Chem.*, 2014, **767**, 136-143.
8. S. Herrmann, M. Kostrzewa, A. Wierschem and C. Streb, *Angew. Chem. Int. Ed.*, 2014, **53**, 13596-13599.
9. Asahi Chemical Industry Co. Ltd., Japanese Patent JP59200769 A2, 1984; *Chem. Abstr.*, 1984, **102**, 82691.
10. N. Mohamamadi, A. Ganesan, C.T. Chantler and F. Wang, *J. Organometal. Chem.*, 2012, **713**, 51-59.
11. L. Zhang, H. Chen, X. Zhao, Q. Zhai, D. Yin, Y. Sun and J. Li, *Appl. Catal. B: Env.*, 2016, **193**, 47-57.
12. E.S. Yang, M.-S. Chan and A.C. Wahl, *J. Phys. Chem.*, 1980, **84**, 3094-3099.
13. R. Sun, L. Wang, H. Yu, Z. Abdin, Y. Chen, J. Huang and R. Tong, *Organometallics*, 2014, **33**, 4560-4573.
14. M.S. Morad and A.A.O Sarhan, *Corros. Sci.*, 2008, **50**, 744-753.
15. K.-Y.A. Lin, T.-Y. Lin, Y.-C. Chena and Y.-F. Lin, *Catal. Commun.*, 2017, **95**, 40-45.
16. T. Daeneke, T. Kwon, A.B. Holmes, N.W. Duffy, U. Bach and L. Spiccia, *Nat. Chem.*, 2011, **3**, 211-215.
17. R.H. Palmer, J. Liu, C.-W. Kung, I. Hod, O.K. Farha and J.T. Hupp, *Langmuir*, 2018, **34**, 4707-4714.
18. M. (Thor) Pope, *Heteropoly and Isopoly Oxometalates*, Springer-Verlag, Berlin, Heidelberg, 1983.
19. K. Shakeela, V.L. Sinduri and G. Ranga Rao, *Polyhedron*, 2017, **137**, 43-51.
20. I. Kozhevnikov, *Catalysts for Fine Chemical Synthesis, Catalysis by Polyoxometalates*, Wiley, Chichester, 2002, vol. 2.
21. R. Meenakshi, K. Shakeela, S. Kutti Rani and G. Ranga Rao, *Catal. Letters*, 2018, **148**, 246-257.
22. T. Rajkumar and G. Ranga Rao, *J. Mol. Catal. A Chem.*, 2008, **295**, 1-9.
23. M. Ammam, *J. Mater. Chem. A*, 2013, **1**, 62-91.
24. R. Sivakumar, J. Thomas and M. Yoon, *J. Photochem. Photobiol. C: Photochem. Rev.*, 2012, **13**, 277-298.
25. T. Ueda, *ChemElectroChem*, 2018, **5**, 823-838.
26. L. George, K. Shakeela, G. Ranga Rao and M. Jaiswal, *Phys. Chem. Chem. Phys.*, 2018, **20**, 18474-18483.
27. K. Shakeela, G. Silpa, S. K. Rayala and G. Ranga Rao, *J. Chem. Sci.*, 2018, **130**, 107.
28. K. Shakeela and G. Ranga Rao *ACS Appl. Nano Mater.*, 2018, **1**, 4642-4651.
29. D.E. Katsoulis, *Chem. Rev.*, 1998, **98**, 359-387.
30. H. Xu, Z. Li, B. Liu, G. Xue, H. Hu, F. Fu and J. Wang, *Cryst. Growth Des.*, 2010, **10**, 1096-1103.
31. J. Kang, J.A. Nelson, M. Lu, B. Xie, Z. Peng and D.R. Powell, *Inorg. Chem.*, 2004, **43**, 6408-6413.
32. S. Golhen, L. Ouahab, D. Grandjean and P. Molinie, *Inorg. Chem.*, 1998, **37**, 1499-1506.
33. Z. Li, B. Liu, H. Xu, G. Xue, H. Hu, F. Fu and J. Wang, *J. Organomet. Chem.*, 2009, **694**, 2210-2216.
34. Y. Yan, B. Li, Q. He, Z. He, H. Ai, H. Wang, Z. Yin and L. Wu, *Soft Matter*, 2012, **8**, 1593.
35. J.N. Barrows, G.B. Jameson and M.T. Pope, *J. Am. Chem. Soc.*, 1985, **107**, 1771-1773.
36. M. Jiang, D. Zhu, H. Zhang and X. Zhao, *New J. Chem.*, 2014, **38**, 3354-3357.
37. C. Tan and W. Bu, *J. Solid State Chem.*, 2014, **219**, 93-98.
38. C. Tan, *J. Mol. Struct.*, 2017, **1148**, 34-39.
39. H. Luo, C. Dong, K. Xiao and X. Lib, *RSC Adv.*, 2016, **6**, 9940-9949.
40. N. Perez, *Electrochemistry and Corrosion Science*, Kluwer Academic Publishers, Massachusetts, 2004, p. 10.
41. K.G.C. Senarathna, H.M.S.P. Randiligama, R.M.G. Rajapakse, *RSC Adv.*, 2016, **6**, 112853-112863.
42. J.A. Prithi, N. Rajalakshmi, G. Ranga Rao, *Int. J. Hydrogen Energy*, 2018, **43**, 4716-4725.
43. P. Justin, P. Hari Krishna Charan, G. Ranga Rao, *Appl. Catal. B: Environ.*, 2014, **144**, 767-774.
44. G. Ranga Rao, T. Rajkumar and B. Varghese, *Solid State Sci.*, 2009, **11**, 36-42.
45. P. Giannozzi, S. Baroni, N. Bonini, M. Calandra, R. Car, C. Cavazzoni, D. Ceresoli, G.L. Chiarotti, M. Cococcioni, I. Dabo, A. Dal Corso, S. de Gironcoli, S. Fabris, G. Fratesi, R. Gebauer, U. Gerstmann, C. Gougoussis, A. Kokalj, M. Lazzeri, L. Martin-Samos, N. Marzari, F. Mauri, R. Mazzarello, S. Paolini, A. Pasquarello, L. Paulatto, C. Sbraccia, S. Scandolo, G. Sclauzero, A.P. Seitsonen, A. Smogunov, P. Umari, R.M. Wentzcovitch, QUANTUM ESPRESSO: a modular and open-source software project for quantum simulations of materials, *J. Phys. Condens. Matter*, 2009, **21**, 395502:1-19.
46. D.-L. Long, E. Burkholder and L. Cronin, *Chem. Soc. Rev.*, 2007, **36**, 105-121.
47. F138, Standard Specification for Stainless Steel Bar and Wire for Surgical Implants (special quality), *Annual book of ASTM Standards*, ASTM, PL, 1992, **13.01**, 22-24.

48. B.D. Viezbicke, S. Patel, B. E. Davis and D. P. Birnie III, *Phys. Status Solidi B.*, 2015, **252**, 1700-1710.
49. E. López-Salinas, J.G. Hernández-Cortéz, I. Schifter, E. Torres-Garcia, J. Navarrete, A. Gutiérrez-Carrillo, T. López, P.P. Lottici and D. Bersani, *Applied Catal. A: Gen.*, 2000, **193**, 215-225.
50. E. Naseri and R. Khoshnavazi, *RSC Adv.*, 2018, **8**, 28249-28260.
51. C.I.R. Magalhaes, A.C. Gomes, A.D. Lopes, I.S. Gonçalves, M. Pillinger, E. Jin, I. Kim, Y.H. Ko, K. Kim, I. Nowikf and R.H. Herber, *Phys. Chem. Chem. Phys.*, 2017, **19**, 21548-21555.
52. C.A. McAuliffe, *Techniques and Topics in Bioinorganic Chemistry*, Mcmillan Press, London, 1975, pp. 242-244.
53. N.T. Kirkland, N. Birbilis, M.P. Staiger, *Acta Biomater.*, 2012, **8**, 925-936.
54. J R Scully, *Corrosion*, 2000, **56**, 199-218.
55. A. Singh, K.R. Ansari, M.A. Quraishi, S. Kaya and P. Banerjee, *New J. Chem.*, 2019, **43**, 6303-6313.
56. H.-S. Lee, J.K. Singh, M.A. Ismail, C. Bhattacharya, A.H. Seikh, N. Alharthi, R.R. Hussain, *Sci. Rep.*, 2019, **9**, 3399.
57. Z. Kerner and T. Pajkossy, *Electrochim. Acta*, 2000, **46**, 207-211.
58. P. Agarwal, M.E. Orazem, L.H. Garcia-Rubio, *J. Electrochem. Soc.*, 1992, **139**, 1917-1927.
59. B.A. Boukamp, *J. Electrochem. Soc.*, 1995, **142**, 1885-1894.
60. V. Otieno-Alego, G.A. Hope, H.J. Flitt, G.A. Cash, D.P. Schweinsber, *Corros. Sci.*, 1992, **33**, 1719-1734.
61. X.L. Zhang, Zh.H. Jiang, Zh.P. Yao, Y. Song, Zh.D. Wu, *Corros. Sci.*, 2009, **51**, 581-587.
62. N. Elgrishi, K.J. Rountree, B.D. McCarthy, E.S. Rountree, T.T. Eisenhart, Jillian L. Dempsey, *J. Chem. Educ.*, 2018, **95**, 197-206.
63. R.A. Buchanan, E.E. Stansbury, in *Handbook of Environmental Degradation of Materials*, ed. M. Kutz, Elsevier, Oxford, 2nd ed., 2012, 4, pp. 87-125.
64. M. Stern, A.L. Geary, *J. Electrochem. Soc.*, 1957, **4**, 56-63.
65. A. Robin, O.A.S. Carvalho, S.G. Schneider and S. Schneider, *Mater. Corros.*, 2008, **59**, 929-933.
66. K.J. Bundy, M.A. Vogelbaum and V.H. Desai, *J. Biomed. Mater. Res.*, 1986, **20**, 493-505.
67. I. Holclajtner-Antunovic, D. Bajuk-Bogdanovic, M. Todorovic, U.B. Mio, J. Zakrzewska and S. Uskokovic-Markovic, *Can. J. Chem.*, 2008, **86**, 996-1004.
68. S. Guru, G. Ranga Rao, *ChemistrySelect*, 2019, **4**, 10884-10894.
69. J. Ruiz, F. Ogliaro, J.-Y. Saillard, J.-F. Halet, F. Varret and D. Astruc, *J. Am. Chem. Soc.*, 1998, **120**, 11693-11705.
70. J.F. Keggin, *Proc. Roy. Soc. A.*, 1934, **144**, 75-100.
71. M. Salet, S. Balula, I.C.M.S. Santos, J.A.F. Gamelas, A.M.V. Cavaleiro, N. Binsted and W. Schlindwein, *Eur. J. Inorg. Chem.*, 2007, **1**, 1027-1038.
72. J. Evans, M. Pillinger and J.M. Rummey, *J. Chem. Soc. Dalton Trans.*, 1996, **1**, 2951-2961.
73. K. Bhrara, G. Singh, *Appl. Surf. Sci.*, 2006, **253**, 846-853.
74. S.K. Saha, A. Dutta, P. Ghosh, D. Sukul and P. Banerjee, *Phys. Chem. Chem. Phys.*, 2016, **18**, 17898-17911.
75. A. Kahn, *Mater. Horiz.*, 2016, **3**, 7-10.